

Extreme Ultraviolet Explorer spectrometer

Michael C. Hettrick, Stuart Bowyer, Roger F. Malina,
Christopher Martin, and Stanley Mrowka

Applied Optics Vol. 24, Issue 12, pp. 1737-1756 (1985)

<http://dx.doi.org/10.1364/AO.24.001737>

© 1985 Optical Society of America. One print or electronic copy may be made for personal use only. Systematic reproduction and distribution, duplication of any material in this paper for a fee or for commercial purposes, or modifications of the content of this paper are prohibited.

Extreme Ultraviolet Explorer spectrometer

Michael C. Hettrick, Stuart Bowyer, Roger F. Malina, Christopher Martin, and Stanley Mrowka

The design and calculated performance is described for a spectrometer included on the Extreme Ultraviolet Explorer (EUVE) astronomical satellite. The instrument is novel in design, consisting of three plane reflection gratings mounted in the converging beam behind a grazing incidence telescope. This configuration is based on new varied line-space (VLS) gratings which have recently been proposed. A sample EUVE grating has been mechanically ruled and experimentally characterized. It recovered over 80% of the theoretical efficiency of perfectly formed grooves, reaching 38% absolute at a wavelength of 114 Å. The grating was used to construct a laboratory spectrographic version of the EUVE spectrometer and recorded the spectrum of helium from 228 to 320 Å. The spectral resolution was $\lambda/\Delta\lambda \sim 2000$ and the image heights were ~ 10 sec of arc. Individual spots were $\sim 25 \times 50 \mu\text{m}$, which is a significant improvement over existing grazing incidence spectrographs. A line profile measurement at 1 Å away from first order 304 Å showed $<1.5\%/Å$ of grating stray light and a rapid decline toward the wings. In visible light, no grating stray or ghost light could be seen. Three flight spectrometer channels in combination span the 70–760-Å band with an effective collecting area of 0.3–1 cm^2 over the 80–600-Å region. The spectrometer has an inherent resolution of $\lambda/\Delta\lambda \sim 300$, but if combined with a worst-case satellite performance will yield a spectral resolution of $\lambda/\Delta\lambda = 110$ –240 and a spatial resolution of 1–2 min of arc. For a 40,000-sec observation, the average 3σ sensitivity to continuum flux is $\sim 2 \times 10^{-27}$ $\text{erg}/\text{cm}^2/\text{sec}/\text{Hz}$. This is a factor of 100 dimmer than a bright known EUV source and is comparable to the sensitivity of the all-sky survey which will be carried out on the EUVE. At a 5σ detection threshold, the spectrometer sensitivity to individual spectral lines is 1 – 4×10^{-3} photons/ cm^2/sec , which is a factor of 50 better than available with the EUVE wide bandpass telescopes. Simulated observations of two known classes of extrasolar EUV sources reveal rich spectra. During a six-month spectroscopic phase, target selection will be conducted by guest investigators chosen by NASA.

I. Introduction

The detection of extrasolar objects emitting in the extreme ultraviolet (EUV)^{1–4} has prompted a dedicated mission to discover and identify these sources. The Extreme Ultraviolet Explorer (EUVE) is a NASA observatory which will conduct the first all-sky survey in the entire EUV band ($\lambda\lambda 100$ – 912 Å).⁵ The scientific data retrieved from this photometric mission will be a catalog of all stellar sources above a limiting magnitude of $\sim 10^{-27}$ $\text{erg}/\text{cm}^2/\text{sec}/\text{Hz}$. The entire celestial sphere will be surveyed in a six-month time period. Approximately 4×10^6 sky bins ($0.1^\circ \times 0.1^\circ$) will be individually scanned, and fluxes will be obtained separately in four spectral bands.

The first exploration of any new spectral region in astronomy has always been accompanied by two events: (1) the discovery of new and serendipitous sources, and (2) the requirement for spectroscopic observations to determine the underlying physical phenomena. The feasibility of EUV spectroscopy on stellar sources has been demonstrated in recent years.^{6–8} In addition to known EUV-emitting sources, such as hot white dwarfs,^{1,2,6–8} the coronas of late-type stars,³ cataclysmic variables,⁴ and planets,⁹ the scientific return expected from spectroscopy on newly discovered sources is particularly high.^{10,11}

In response to this need, NASA has included a spectroscopic phase to the EUVE mission. Immediately following the six-month duration survey, the satellite will be pointed for long integrations on spectroscopic targets. Any object within at least $\pm 45^\circ$ of the celestial equator (ecliptic plane) will be accessible by the spectroscopic instrument. This instrument is contained within an imaging telescope which points in the antisun direction during the survey.

To perform a useful first spectroscopic EUV mission, it was determined that the following performance requirements should be met:

The authors are with University of California, Space Sciences Laboratory, Berkeley, California 94720.

Received 26 December 1984.

0003-6935/85/121737-20\$02.00/0.

© 1985 Optical Society of America.

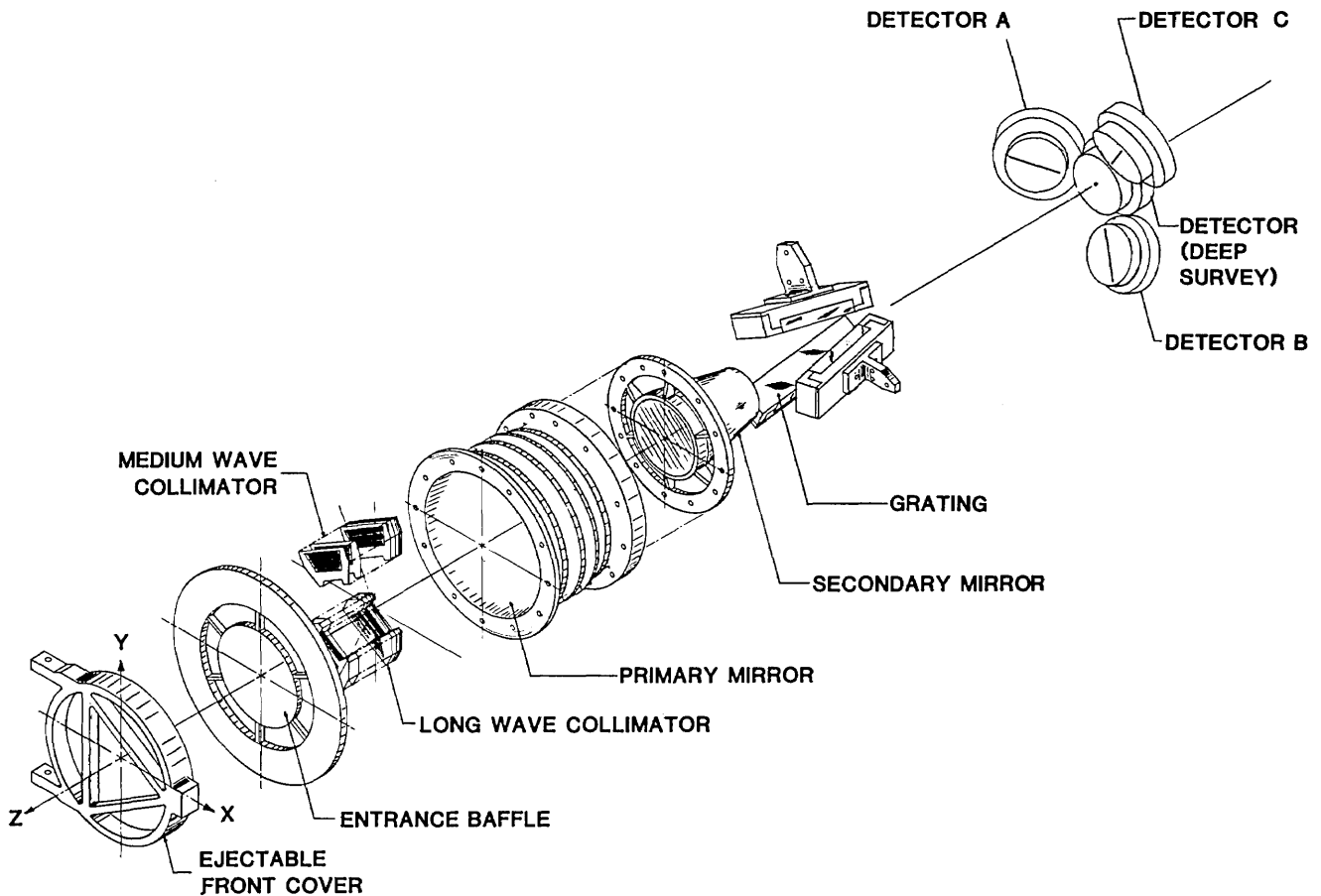


Fig. 1. Exploded view of the EUVE flight spectrometer consisting of three channels which share the telescope aperture.

- (1) simultaneous coverage of the $\lambda\lambda 100\text{--}600\text{-\AA}$ spectral region;
- (2) a spectral resolution $\lambda/\Delta\lambda > 100$;
- (3) a sensitivity 100 times better than necessary to observe the spectrum of the brightest known EUV source HZ43 (a hot white dwarf)¹; and
- (4) sufficiently short exposure times per target (~ 12 h = 40,000 sec) to allow at least 100 separate pointings over a six-month spectroscopy phase.

These scientific requirements were to be met with minimal impact on the EUVE survey mission. This required meeting the following constraints: (a) use of a single grazing incidence telescope with a 40-cm diam aperture to collect the incident starlight; (b) simultaneous sharing of this telescope aperture with a deep survey imaging channel; (c) an image size requiring satellite pointing reconstruction no finer than 1-min of arc sky bins; (d) a minimum overall length for the telescope plus spectrometer, not to exceed ~ 150 cm; (e) use of existing 50-mm microchannel plate imaging detectors having 100- μm pixels; and (f) no moving components.

II. General Approach

Several design options were investigated.¹² Concave grating spectrometers¹³⁻¹⁷ were considered and found to violate our length constraint due to the requirement of a slit. In addition, the sensitivity would be degraded

at grazing incidence due either to large astigmatism or the need for additional correcting elements.^{18,19} Transmission grating spectrometers²⁰⁻²⁶ were carefully studied but found to yield lower efficiency than reflection gratings. Practical limits on groove densities ($< 10^4$ mm^{-1}) resulted in a common disadvantage in resolution for both transmission gratings and conical diffraction reflection gratings. Other approaches^{27,28} were found to be inconsistent with either the deep survey instrument or the intended EUVE spectroscopy mission. On the basis of spectral resolution, sensitivity, instrument packaging, and technical feasibility, we converged to a slitless design employing new varied line-space grazing incidence gratings.^{29,30}

In Fig. 1 we show an exploded view of the spectroscopy instrument. Incident starlight is collected by a grazing incidence telescope. Following reflection by the primary and secondary mirror elements, the light converges as an annular cone to a focus on the deep survey detector, which uses half of the aperture. The remaining half of the light is devoted to spectroscopy, which is accomplished through the presence of three plane reflection gratings in the converging beam. Each grating picks off one-sixth of the collected light and defines a channel spanning approximately one octave in EUV wavelength. The combined coverage extends over the 70-760- \AA region and provides highest efficiency

(>50% of peak) in the 80–600-Å range. The channels are separately optimized by appropriate choice of grating groove densities, reflective coatings, and filters but are otherwise geometrically identical. Each grating features a smoothly varying line (groove) spacing across its aperture, which constrains the diffracted beams to form a well-imaged spectrum. The use of varied line-spacing (VLS) in converging light also results in excellent spatial imaging normal to the dispersion.²⁹ Each of the three spectra is imaged on a dedicated microchannel plate imaging detector with a flat surface normal to the diffracted light. To suppress undesirable background, dominantly the diffuse sky at hydrogen Ly α (1216 Å) and starlight in the far UV, each detector is preceded by a thin-film filter. In addition, field-restricting collimators placed in front of the telescope prevent EUV lines in the diffuse sky (304 and 584 Å) from contaminating the entire spectrum.

A cross section of the instrument is shown in Fig. 2. The optical path is indicated for one of the three spectroscopy channels. The use of VLS gratings in this unconventional converging beam geometry results in a total of only three optical surfaces. As each one is at grazing incidence, a highly efficient instrument is realized.

III. Detailed Instrument Design

In Table I we list the major design parameters of this instrument. The optimum spectrometer performance is a balance between several contributions, as shown in Fig. 3. In this section we describe the individual components of the spectroscopy instrument and their effects on the instrument resolution and efficiency. These two principal criteria for performance are sufficiently decoupled to permit separate optimization, however both determine the ultimate sensitivity achieved.

The dominant aberrations are specified to correspond to a blurring no more than 1 min of arc of sky. This specification is driven both by the practical constraints outlined in Sec. I and by the fact, derived below, that an optimized design will convert this error into an acceptable spectral resolution of $\lambda/\Delta\lambda \sim 200$. In addition, a 5σ sensitivity level of 10^{-3} photons/cm²/sec over a 40,000-sec observation translates to an effective area of 0.3 cm², assuming background is not the limiting factor. This requirement will imply an instrument efficiency >0.5%, including the detector.

A. Telescope

This optical component both collects and focuses the incident radiation. It is primarily responsible for the overall physical size of the instrument and its collecting area and indirectly determines the resolution delivered by the grating and detector. Longer focal lengths produce more slowly converging beams and thus reduce grating aberrations and the sky pixel blurring arising from finite detector pixel sizes. However, given a telescope resolution, longer focal lengths also result in larger images at the detector. Given our fixed aperture, these competing effects result in an optimum value for the focal length, which we calculate to be ~ 136 cm for

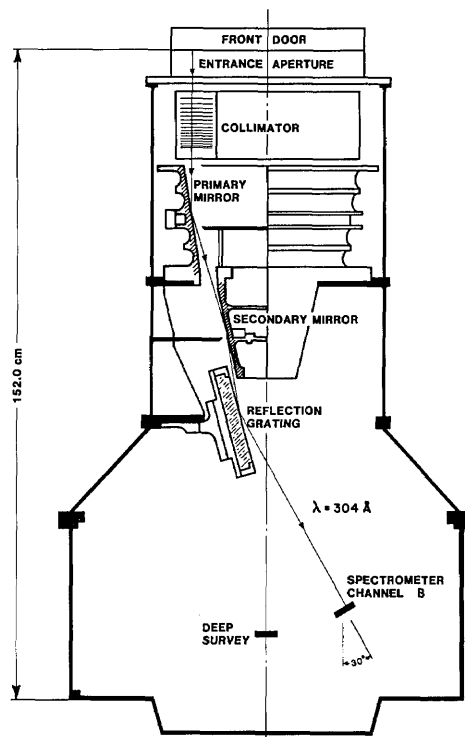


Fig. 2. Cross-sectional view of the flight spectrometer illustrating the three grazing reflections. The optics for one of three grating channels are shown with the optical path of a 304 Å photon. The mechanical collimator acts as a field-limiting slit.

Table I. EUVE Spectrometer Characteristics

| | |
|--|--|
| Performance: | |
| Spectral channels (simultaneous) | A, 70–190 Å B, 140–380 Å C, 280–760 Å |
| Spectral resolution (averages) | A, 0.5 Å B, 1.0 Å C, 2.0 Å |
| Spatial resolution | 1.5 min of arc |
| Effective area (80–600 Å) | 0.4 cm ² |
| Collecting optics: Wolter-Schwarzschild type-2 | |
| Aperture | 40-cm diameter |
| Speed | $F/3.4$ |
| Reflective coating | Gold |
| Grating: varied line-space in-plane mounting | |
| Plate scale (averages) | A, 2.4 Å/mm B, 4.8 Å/mm C, 9.6 Å/mm |
| Groove density variations | A, 1675–3550 mm ⁻¹ B, 830–1750 mm ⁻¹ C, 415–875 mm ⁻¹ |
| Plane surface ruled area | 80 × 200 mm |
| Blaze angle | 3.0° |
| Angle of incidence (average) | 82.9° |
| Reflective coating | Rhodium |
| Detector: microchannel plate | |
| Aperture | 50-mm diameter |
| Resolution | 100 × 100 μm |
| Filters | A, 0.3-μm Parylene-N B, 0.15-μm aluminum C, 0.15-μm aluminum |
| Photocathode | Cesium iodide |

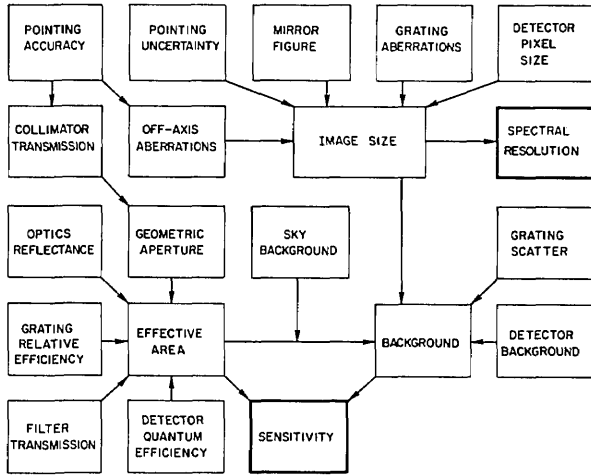


Fig. 3. System block diagram showing the contributions from several factors to the instrument resolution and sensitivity.

the spectroscopy instrument. To minimize the instrument length while maximizing the collecting aperture we chose a Wolter-Schwarzschild type-2 telescope,³¹ whose surface functions are described by the parametric equations:

$$z_1 = -F/C_1 + (FC_1/4) \sin^2\beta + (F/C_2) \times [1 - C_1 \sin^2(\beta/2)]^{(2-C_1)/(1-C_1)} \times [\cos(\beta/2)]^{2C_1/(C_1-1)}, \quad (1a)$$

$$r_1 = F \sin\beta, \quad (1b)$$

$$z_2 = d \cos\beta, \quad (1c)$$

$$r_2 = d \sin\beta, \quad (1d)$$

where

$$1/d = (C_1/F) \sin^2(\beta/2) + (C_2/F) [1 - C_1 \sin^2(\beta/2)]^{C_1/(C_1-1)} \times [\cos(\beta/2)]^{2/(1-C_1)}, \quad (1e)$$

In these equations, β is the parameter which identifies a particular ray assumed incident in a direction parallel to the optical axis of the telescope. The value of β is the angle such a ray will make with the optical axis on exiting the telescope. The ray intersections with the primary and secondary mirrors are given by radial coordinates r_1 and r_2 and by axial coordinates z_1 and z_2 from the focus. The dimensionless parameters C_1 and C_2 specify a particular solution for this mirror system. A useful feature of this telescope results from its ability to fold a desired focal length into a short physical length. In our case, we chose a front-to-focus length $z_{\max} = 107$ cm, which left adequate space for the collimators and for the detector electronics. This results in dimensionless parameters $C_1 = 132$ and $C_2 \approx 3.5$. To feasibly limit the required grating sizes, we chose a primary mirror aperture extending in radius from 16 to 20 cm, yielding $\beta \approx 0.1178-0.1474$. The axial length of the primary mirror is ~ 28 cm. Incident rays parallel to the optical axis strike the mirror surfaces at mean graze angles (area weighted) of 9.3° for the primary and 5.6° for the secondary. These angles are sufficiently small to allow high reflection efficiencies to wavelengths somewhat below 100 \AA .

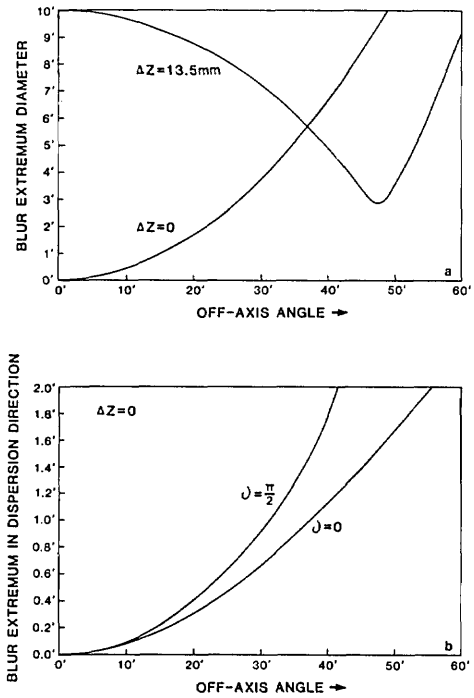


Fig. 4. Telescope off-axis aberrations for (a) entire telescope and (b) section devoted to a spectrometer channel. A defocusing of the detector by a distance ΔZ allows the field to be widened. The angle ν is that between the grating dispersion and the direction in which an incident ray is off-axis. The image is elongated in the nondispersive direction independent of ν .

Ray traces of this telescope are shown in Fig. 4(a) for full surfaces of revolution and a flat detector surface normal to the optical axis. At this Gaussian focus, the extremum image diameters are well described by

$$D(\theta) = \chi\theta^2, \quad (2)$$

where θ is the off-axis (field) angle of a point source, χ is ~ 14.3 , and D , θ are in radians. The deep survey instrument (which shares half of the telescope aperture) has an imaging requirement of 0.1° , permitting a 1.5° field of view. Figure 4(a) also illustrates that, if the detector was displaced 13.5 mm toward the telescope, the on-axis image would be defocused to a 10-min of arc diameter, and the off-axis aberrations would be kept below this over a 2.1° field. The latter matches the detector aperture of 50 mm.

However, the telescope must image to better than 0.5 min of arc in order not to dominate the spectrometer aberrations. This requirement is a factor of 12 tighter than that of the deep survey. Fortunately, only one-sixth of the telescope aperture is used for any one spectrometer channel, resulting in greatly reduced field aberrations. As shown in Fig. 4(b), the aberration in the grating dispersion direction is < 0.5 min of arc if the off-axis angle θ is $< 0.5^\circ$. [This corresponds to $\chi \approx 3.3$ in Eq. (2), although the actual dependence of aberration on off-axis angle is no longer purely quadratic.] Thus, to maintain tolerable off-axis aberrations, the telescope optical axis need not be pointed very accurately toward a spectroscopy target. Defocusing of the on-axis image is not necessary and would in any case yield marginal

gain due to the high degree of focal curvature for the W-S type-2 telescope.

A final consideration is the residual size of an on-axis stellar image due to fabrication imperfections of the telescope, i.e., its figure. Recent visible light measurements being reported³² for an EUVE scanning mirror reveal the on-axis imaging to be better than 2-sec of arc FWHM (full width at half-maximum) and 5-sec of arc HEW (half-energy width). Similar results are expected for the spectroscopy telescope and represent a negligible contribution to the error budget.

B. Gratings

The heart of this spectroscopy instrument is the array of three reflection gratings located directly behind the telescope. A detailed view of any one such grating mount is shown in Fig. 5. The general principle on which this unusual mount is based^{29,30} is to allow the telescope to provide most of the focusing power and use the grating to provide the wavelength dispersion and fine corrections to the residual aberrations. A plane grating surface is chosen, thereby removing the large astigmatic aberrations present with the conventional spherical surface at grazing incidence. A plane grating yields a pointlike stigmatic image in zero order when illuminated by convergent light. A defining feature of these plane gratings is the smooth variation in groove spacings which removes the dominant residual aberrations over a wide field centered on a preselected wavelength (λ_*). The grating is used in an otherwise classical in-plane mounting and features grooves which are both straight and parallel to each other. At grazing incidence, the required space variation is approximately proportional to the square of the glancing angle (α). The precise variation is given by the grating equation:

$$d(x) = m\lambda_* / [\cos\beta_*(x) - \cos\alpha(x)], \quad (3)$$

where x is the ruled width. The groove spacing $d(x)$ is approximately a polynomial.²⁹ The incident and diffracted angles, α and β , are relative to the grating tangent as shown in Fig. 5; β_* is the angle diffracted to a fixed detecting position for λ_* .

To minimize the (dominant) aberration arising from instrument pointing uncertainties, we have chosen to use the inside spectral order ($m = -1$). At grazing incidence, this results in a significant deamplification of any image blur $\Delta\theta$ (FWHM) introduced prior to the grating. This is observed through inspection of the dispersive limit to the attainable spectral resolution³⁰:

$$\lambda/\Delta\lambda = |\beta/\alpha_0 - 1| \sin\gamma_0 / (F/L_0) / \Delta\theta, \quad (4)$$

where L_0 is the central grating-detector separation, γ_0 is the reflection graze angle relative to the central groove, and β and α_0 are derived from Eq. (3). At the central wavelength for each channel, $\beta/\alpha_0 \sim 2$ for the inside order (whereas $\beta/\alpha_0 \sim 1/2$ if the outside order were chosen). Inserting the other parameters ($\gamma_0 = 10^\circ$, $F/L_0 = 2.8$) yields a resolution $\lambda/\Delta\lambda = 250$ for $\Delta\theta = 1$ min of arc. This value may be understood in terms of

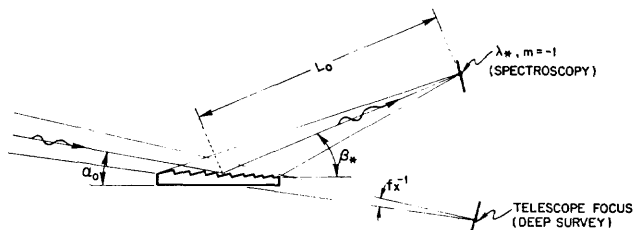


Fig. 5. Grating mounting using a converging beam of incident light.

the plate scales. Given detectors each with an aperture of 50 mm, the three gratings cover the wavelength ranges 70–190 Å, 140–380 Å, and 280–760 Å. (The correction wavelengths λ_* are 160, 320, and 640 Å, and the wavelengths striking the detector center are 125, 250, and 500 Å, respectively.) The average plate scales are therefore 2.4, 4.8, and 9.6 Å/mm in the three channels. A 1-min of arc image produces an image diameter of 0.4 mm at the focal plane of the telescope ($F = 1361.4$ mm). However the deamplification ratio of $\beta/\alpha_0 \sim 2$ results in a width of only 0.2 mm in the dispersion direction for the first-order image. Thus, the grating plate scales are translated into $\sim 0.5, 1.0,$ and 2.0 Å/min of arc for the three channels. At the center of each channel, a resolution of $\lambda/\Delta\lambda \sim 250$ is thereby attainable if $\Delta\theta = 1$ min of arc. This dominates other contributions to the resolution budget, being larger than the telescope imaging ($\Delta\theta = 0.25$ min of arc, $\lambda/\Delta\lambda = 1000$), the detector pixel size (0.1 mm, $\lambda/\Delta\lambda = 500$), and even the grating aberrations ($\lambda/\Delta\lambda = 350$) as shown below.

In each of the grating mounts, α increases from 6.02° to 8.62° over a ruled width of 173.2 mm, resulting in groove densities which vary over ~ 415 –840, 830–1675, and 1650–3350 mm^{-1} for the long, medium, and short wavelength channels, respectively. To intercept off-axis rays, the flight gratings will have a ruled width of 200 mm.

1. Imaging Properties

The spectral resolution attainable by such a grating is determined by the speed f_y of the incident light along the direction of the groove heights:

$$\lambda_*/\Delta\lambda_* = 8f_y^2. \quad (5)$$

However, the image height H in the direction normal to dispersion depends also on f_x across the ruled width:

$$H/L(0) = |m\lambda_*/d(0)| / (2\alpha_{\max} f_x f_y), \quad (6)$$

where $L(0)$ is the distance from grating center to telescope focus. For the flight spectrometers, $f_y = 6.2$, resulting in a predicted extremum aberration $\lambda/\Delta\lambda = 350$ at λ_* . The remaining parameters are $|m\lambda_*/d(0)| = 0.037$, $L(0) = 485.5$ mm, and $f_x = 22$, resulting in a predicted image height of only 0.4 mm. This is equivalent to 1 min of arc of telescope aspect.

In Fig. 6 we show the results of ray tracing the medium wavelength channel ($\lambda\lambda 140$ –380 Å). In these calculations we have optimized the use of a plane detector

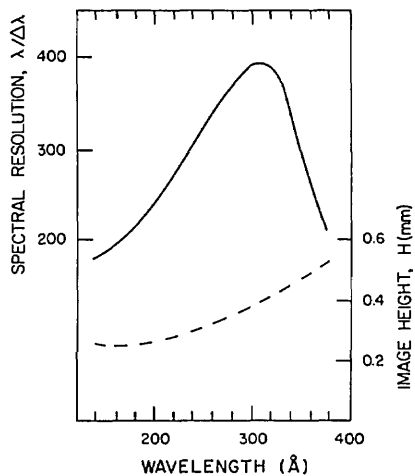


Fig. 6. Geometrical aberrations of the short wavelength flight grating derived from numerical ray tracings of the extremum image sizes. A spectral resolution of $\lambda/\Delta\lambda = 300$ and an image height of 0.35 mm are typical values.

surface for wide spectral coverage. This was achieved by orienting the detector normal to lie exactly along the ray diffracted from grating center to detector center (250 Å). The detector is thereby found to make an angle of 15.5° with the grating normal and 30.0° with the optical axis of the telescope. As seen in Fig. 6, a spectral resolution of $\lambda/\Delta\lambda = 200$ – 350 is obtained simultaneously with a spatial resolution of $H = 0.2$ – 0.4 mm over the 140–380-Å range in wavelength. Off-axis illumination of the grating (due to telescope pointing errors) must also be considered. However, over the specified field of ± 15 min of arc, the deviations between the optimal focal surfaces of the telescope and the grating are small, resulting in only an overall shift in the absolute wavelength scale³⁰ (15 Å).

Employing the flight mounting parameters, we have experimentally verified the imaging properties of a sample grating which was mechanically ruled by Hitachi using the technique of Harada and Kita.³³ Electron micrographs of this test grating appear in Fig. 7, showing both the low (1400-mm^{-1}) and high (1800-mm^{-1}) density regions. This grating is a 50-mm section of the medium wavelength flight grating. The blaze angle was specified to be 3.0° .

In Fig. 8 we show a schematic diagram of the instrument used to test the imaging properties of the grating. In Fig. 9 we show the actual experimental apparatus. An entrance slit or pinhole is placed at the exit of a grazing incidence monochromator fed by a Paresce hollow cathode source.³⁴ A converging beam is provided by a small (~ 25.4 -mm diameter) normal incidence spherical mirror placed 3000 mm from this entrance. As the mirror has a 2000-mm radius of curvature, the beam is refocused at a distance of 1500 mm with a focal speed of $\sim f/60$ in all directions. The 50×50 -mm grating is illuminated across 40 mm of its ruled width and partially illuminated (~ 7 mm) along its grooves. Film sensitive to ultrasoft x rays,³⁵ Kodak 101-06, was placed at the focal plane chosen for the flight spec-

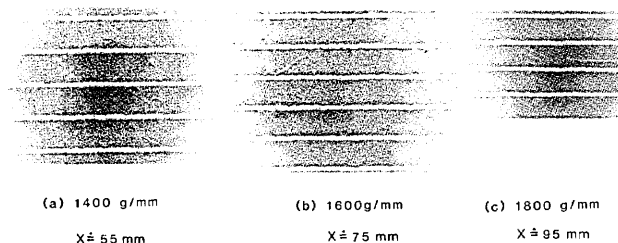


Fig. 7. Electron micrographs of the varied line-space test grating for the EUVE fabricated by Hitachi using a mechanical ruling engine. The groove spacings vary smoothly from 1400 to 1800 grooves/mm across a 48-mm ruled width. The ruled width is in the vertical direction in this figure, and three small sections are relocated side-by-side for comparison. The blaze angle is $\sim 3.0^\circ$. These electron micrographs were taken for an aluminum replica prior to overcoating with rhodium.

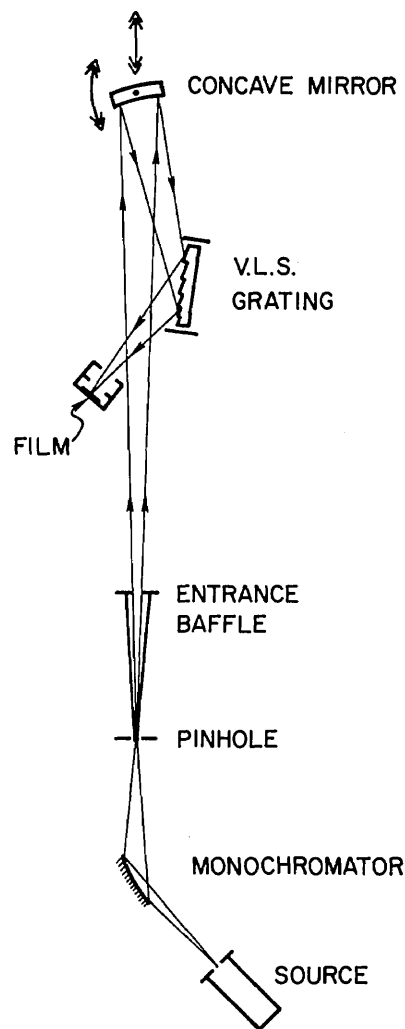


Fig. 8. Schematic of a laboratory spectrograph used to test the the imaging proeptrties of the EUVE test grating.

trometer. The spherical mirror functions as the collecting optic in this system and is coated with osmium for which usable reflectance is expected to extend somewhat below 300 Å.

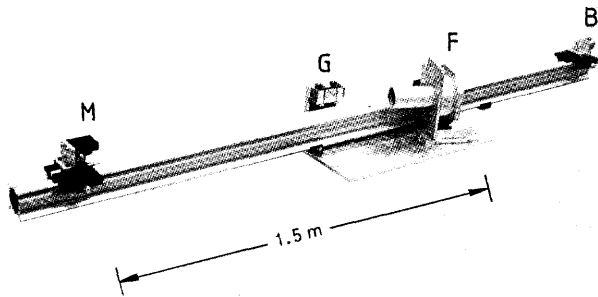


Fig. 9. Photograph of the laboratory spectrograph used to test the imaging of a varied-space grating. The spherical mirror (*M*), test grating (*G*), and film (*F*) are mounted on a common optical bench. The source of light enters from a pinhole preceding the entrance baffle (*B*), as shown in Fig. 8.

To obtain a polychromatic spectrum of the source and thus to demonstrate the grating resolution, the monochromator was switched to zero order, and the spectrometer entrance slit set to 0.1×2 mm. The spectrum we obtained (Fig. 10) shows an intense $304\text{-}\text{\AA}$ line and a series approaching 228 \AA . This is the Lyman series for ionized helium, the gas for which the source was operating. An additional line at 320 \AA , due to neutral helium, is also observed. By overexposing this spectrum, we were able to detect a cluster of neutral helium lines from 290 to 310 \AA , revealing a resolution in excess of 1000.

However, the spectral resolution and image heights shown in Fig. 10 are due to the large dimensions of the entrance slit. To test the inherent resolution of our optical system, we replaced this slit by a $25\text{-}\mu\text{m}$ diam pinhole. In Fig. 11 we show the recorded image at 304 \AA , for which computer simulations predict a $20 \times 20\text{-}\mu\text{m}$ spot including the aberrations of the spherical mirror at 1° off-axis. The measured resolution, including vibration of the fixture in the vacuum chamber ($<30\text{ }\mu\text{m}$) and film resolution ($\sim 5\text{ }\mu\text{m}$), is $22\text{ }\mu\text{m}$ in the dispersion direction and $58\text{ }\mu\text{m}$ in height. Given the known plate scale ($5\text{ \AA}/\text{mm}$), the image width converts to a spectral resolution $\lambda/\Delta\lambda \sim 2500$. The image dimensions are equivalent to an incident beam of angular divergence 7×9 sec of arc. The recorded image at 256 \AA (Fig. 11) shows dimensions of $53\text{-}\mu\text{m}$ width by $75\text{-}\mu\text{m}$ height. Thus, even far away from the correction wavelength ($\lambda_* = 316.4\text{ \AA}$) the images remain small in both dimensions.

2. Stray Light

The imaging apparatus also provided an efficient method of obtaining the distribution of focused stray light (FSL) near the first-order image. To obtain the halo of the $304\text{-}\text{\AA}$ image, we overexposed the spectrum shown in Fig. 10, and we show in Fig. 12 a microdensitometer trace in the dispersion direction. We determined the total $304\text{-}\text{\AA}$ intensity by the measured relative intensities of all lines in an unsaturated exposure and using the film calibration given by Henke *et al.*³⁵ The horizontal axis of Fig. 12 corresponds to the wavelength plate scale at the detector, and thus the vertical

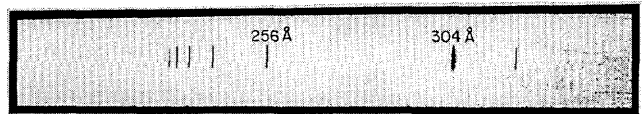


Fig. 10. Spectrum recorded by the laboratory spectrograph showing the HE II Lyman series. The image heights (~ 1 mm) are due to the dimensions of an entrance slit rather than due to the grating or optical system. The dim features near the bright $304\text{-}\text{\AA}$ image are lines of neutral helium, as is the $320\text{-}\text{\AA}$ image to the far right. No ghost lines are detectable in the spectrum.

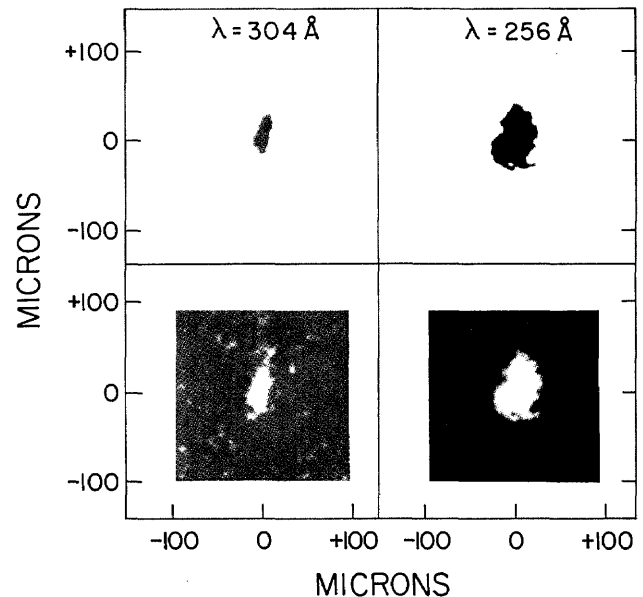


Fig. 11. Recorded images of 304 and 256 \AA using an entrance pinhole of $25\text{-}\mu\text{m}$ diameter. The image widths are $\sim 20\text{--}50\text{ }\mu\text{m}$ and the heights are $\sim 50\text{--}80\text{ }\mu\text{m}$. The upper panels are high contrast reproductions showing only the brightest regions of the images.

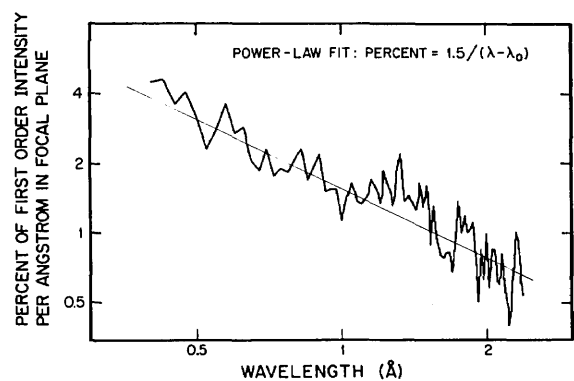


Fig. 12. Microdensitometer profile of stray light in the halo of an overexposed $304\text{-}\text{\AA}$ line image. Due to unknown contributions from the entrance slit width and the film image halo, this light level is an upper limit to that produced by the grating.

scale is in units of percent per angstrom. This profile is well described by the formula

$$\omega(\text{\AA}^{-1}) = 0.015|\lambda - \lambda_0|^{-1}, \text{ for } 0.3\text{ \AA} < |\lambda - \lambda_0| < 3\text{ \AA}. \quad (7)$$

This has not been corrected for either the wide entrance

slit ($\sim 0.3\text{-}\text{\AA}$ halfwidth), the contribution of diffraction from the finite optical apertures, or the contribution from image broadening of overexposed film. Thus, it is an upper limit to the grating scatter but is still only 1.5% of the first-order intensity of 304 \AA within a $1\text{-}\text{\AA}$ bin located 1 \AA from the line center. Due to limitations of this method, the FSL level could not be obtained in the wings of the profile, however some qualitative information was obtained in the visible (6328 \AA) through pencil-beam illumination. Neither stray line nor ghosts could be seen, in contrast to easily visible levels produced by conventional gratings ruled on other engines. A varied line-space concave grating ruled on the same engine and having a similar line spacing and ruled width has been reported³⁶ to scatter $<10^{-5}\text{ \AA}^{-1} = 10^{-3\%}\text{ \AA}^{-1}$ at 100 \AA from the line center at 304 \AA . For comparison,³⁷ at 1236 \AA a photoresist grating has been reported at the same level and a conventionally ruled grating at $\sim 2 \times 10^{-2\%}\text{ \AA}^{-1}$.

3. Efficiency

We have also made detailed efficiency measurements on the test grating. To enhance the EUV reflectance, the replica grating (aluminum surface) was overcoated with 125 \AA of rhodium over a binding layer of $50\text{-}\text{\AA}$ chromium. Reflectance values reported in the literature³⁸⁻⁴¹ reveal an improvement for rhodium over other standard coatings (e.g., gold or platinum) in the region of interest ($\lambda \sim 100\text{-}600\text{ \AA}$).

Monochromatic pencil-beam radiation was provided by a Henke tube,⁴² a Penning source,⁴³ or a hollow cathode source³⁴ placed at the entrance slit of a grazing incidence monochromator. These sources provided lines at 114 \AA , 170 \AA , and at $256, 304, 584,$ and 1216 \AA , respectively. The intensities of the diffracted images were measured by translating the grating into the beam and positioning the detector of intercept the diffracted orders (e.g., $m = 0, 1, 2,$ etc.). To minimize variations in detector efficiency, the image was always centered on the detector and incident at a fixed angle to the microchannels. The grating was positioned by translating it across the incident beam and monitoring the reflected signal to locate the grating center. Aperture stops ensured that the grating would then be underilluminated. Since the detector was an imaging microchannel plate, histograms of the accumulated counts were also monitored to ensure that one (and only one) spectral order fell safely within the field of view. Spectral impurities of the monochromator were removed by switching to a nearby (off-line) background region and subtracting the counts. All counts were corrected for electronic dead times ($<10\%$ in all cases). Absolute grating efficiencies were obtained by normalizing these results to the incident beam intensity. This intensity was obtained by removing the grating and positioning the detector to intercept the beam directly. The intensity was monitored as a function of time and the results used to correct for temporal drifts (of the order of 1% between measurements).

Measurements were made at several wavelengths and angles of incidence. We show in Fig. 13(a) the absolute

efficiencies as functions of wavelength. These were made with incident light at an 8.4° angle relative to the grating tangent, this being the mounting configuration of the flight gratings for this illuminated section of the ruled width. The first-order efficiencies are seen to rise toward shorter wavelengths, reaching 38% absolute at 114 \AA . This trend is explained in part on the basis of a peak in the diffraction efficiency near the blazed wavelength:

$$\lambda_B \simeq 2d \sin\delta \sin\gamma, \quad (8)$$

where δ is the grating blaze angle and γ is the graze relative to the grating facets. In the negative orders, $\gamma = \alpha + \delta$. The blaze angle was specified to be 3.0° in the sample grating and the nominal groove spacing to be $1/1600\text{ mm}$, resulting in $\lambda_B \simeq 130\text{ \AA}$.

In addition, the reflectance of rhodium is apparently increasing as the wavelength decreases from ~ 200 to 100 \AA , judging by the sum of efficiencies in all observable orders [upper data in Fig. 13(a)]. These values are in excellent agreement both with reflectance values reported by Cox *et al.*³⁸ and those which we have obtained on a flat coated as a witness sample to the grating, using the 11.4° graze angle relative to the groove facets. The grating reflectance of 77% we measure at 114 \AA is in precise agreement with the 76% value we measure for the flat. Assuming a perfectly smooth surface, the optical constants given by Henke *et al.*³⁹ predict a reflectance of 93% .

The relative grating efficiencies are therefore confidently derived as the ratio of the measured absolute efficiency to the measured sum of efficiencies in all orders. In Fig. 13(b) we show this result, revealing relative first-order efficiencies as large as 50% . We find these results to be in excellent agreement with the theoretical efficiency curve given by

$$e_{\text{rel}}(\lambda, m) = I(\lambda, m) / \sum_{\text{all } m} I(\lambda, m), \quad (9a)$$

where

$$I(\lambda, m) = [\sin(\rho_m)/(\rho_m)]^2 / \sin[\beta(\lambda, m)], \quad (9b)$$

$$\rho_m = (\pi g/\lambda) [\cos(\alpha + \delta) - \cos[\beta(\lambda, m) - \delta]] \quad (9c)$$

are the familiar Kirchhoff/Rowland results^{44,45} for diffraction from a reflecting facet of width g . As shown in Fig. 14(a) our grazing incidence mounting results in significant shadowing of the incident light by adjacent grooves, yielding an illuminated width

$$g = d \cos\delta [1 - \tan\delta / \tan(\alpha + \delta)]. \quad (10)$$

Equations (9)–(10) represent a normalized scalar Kirchhoff approximation for the grating relative efficiencies. We note that the $1/\sin\beta$ term in Eq. (9b) accounts for the width of the interference patterns from a given number of grooves and that $\beta(\lambda, m)$ is derived from the grating Eq. (3) in which for the present analysis we treat the spacing d as a constant. This theory predicts a blaze efficiency of $\sin\alpha/\sin\beta$, which has been verified experimentally⁴⁶ and is in agreement with more rigorous theory.⁴⁷ This factor also has a simple geo-

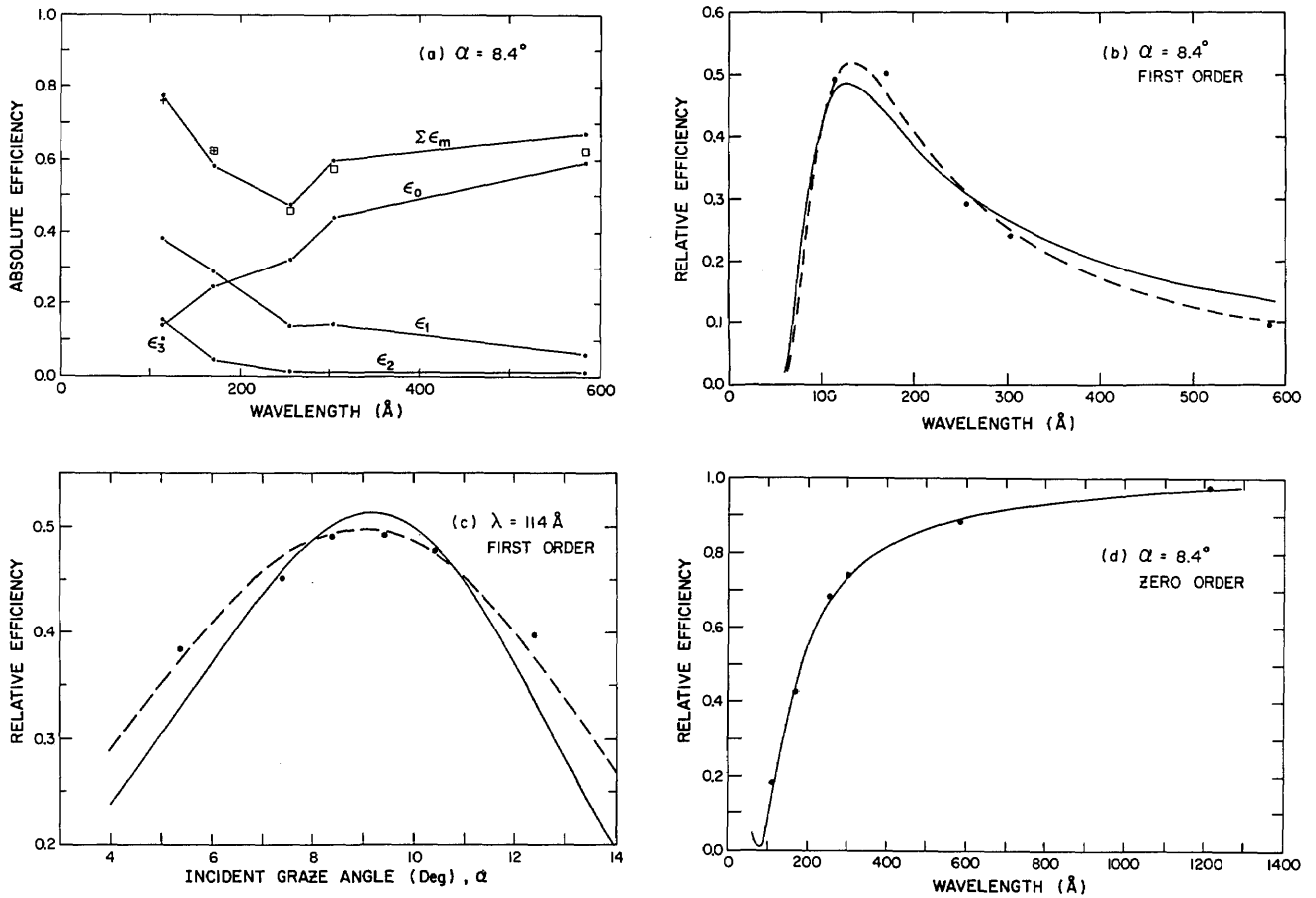


Fig. 13. Measured grating efficiencies. (a) Absolute efficiency in spectral orders 0, 1, 2, and 3 vs wavelength at an 8.4° graze angle to the grating tangent (11.4° to groove facets). The sum $\Sigma \epsilon_m = \epsilon_0 + \epsilon_1 + \epsilon_2 + \epsilon_3$ is compared to our reflectance measurements at 11.4° of a flat witness sample (+) and those found in Ref. 38 (□). (b) Relative first-order efficiencies derived from the left-hand panel compared to theoretical curves times ~ 0.9 . (c) Relative first-order efficiencies vs angle at $\lambda = 114 \text{ \AA}$ compared to theoretical curves times ~ 0.85 . (d) Zero-order relative efficiencies vs wavelength at an 8.4° graze angle compared to a theoretical curve times 1.06.

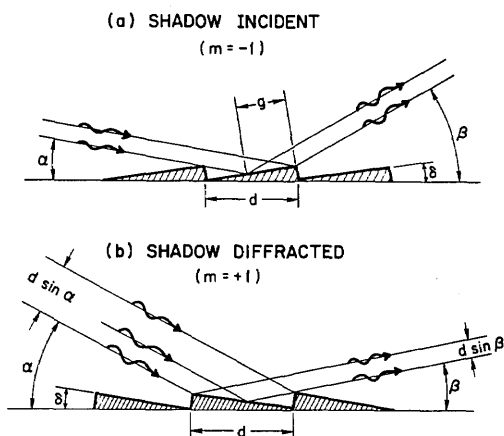


Fig. 14. Geometry of groove shadowing: (a) blaze of an inside spectral order, (b) blaze of an outside spectral order. Shadow factors derived from these geometries may be used to accurately determine the blaze efficiency.

metric interpretation. If the incident and diffracted directions are interchanged [Fig. 14(b)], an appeal to the theorem of optical reciprocity^{48,49} maintains the same absolute grating efficiency at that wavelength. At blaze, the new incident angle β grazes the facet at the same angle ($\beta - \delta$) as in the previous case ($\alpha + \delta$). Therefore, the reflection coefficient is unchanged and the relative efficiency at blaze is equal to that fraction Q of the exiting beam which is not blocked by the adjacent facet:

$$Q = [1 - \tan \delta / \tan(\alpha + \delta)] / [1 + \tan \delta / \tan(\beta - \delta)] \quad (11a)$$

$$= \sin \alpha / \sin \beta, \text{ for } \beta = \alpha + 2\delta. \quad (11b)$$

However, away from the blaze the efficiency curve is more difficult to infer from geometrical arguments, as evidenced by the several variations in this application of the Kirchhoff theory which have been proposed.⁵⁰⁻⁵⁴ Nonetheless, we find our method generates curves in good agreement with the measured efficiencies to within the domain of validity of the Kirchhoff theory.

Using Eqs. (9)-(10), the theoretical first-order curve which best fits the data plotted in Fig. 13(b) is for a blaze angle $\delta = 3.5^\circ$ and for 90% of the theoretical values. As

an alternative (dashed) theoretical curve, we have used simply the shadow factor of Eq. (11a) and the unnormalized diffraction pattern for fully illuminated facets [$g = d$ in Eq. (9c)]. In this case a best fit to the data yields a blaze angle of 3.0° and 82% of the theoretical values. It is remarkable that, with either fit, the data attain over 80% of the theoretical efficiency values. This close agreement with the values expected from perfect grooves is startling, given that we are illuminating the groove tips and have ignored edge defects in the calculations. The worst fit is for data taken at 584 Å, which may be an indication of the breakdown expected in the Kirchhoff theory for effective wavelengths comparable to the groove spacings. For graze angles of 8.4° , the effective wavelength at 584 Å divided by the groove spacing (6250 Å) is ~ 0.7 , while the Kirchhoff theory is valid only for ratios less than ~ 0.4 .^{48,55} Indeed, at 1216 Å ($\lambda_{\text{eff}}/d \simeq 1.35$) the theory predicts a relative efficiency of 4%, whereas a single measurement at this wavelength yielded only $\sim 1.2\%$. In addition, strong polarization effects occur at the longer wavelengths, which this scalar theory neglects, and the reflection coefficient there should be derived from a generalized Fresnel equation.⁵¹ Neglected effects which are not expected to be significant include polarization of the incident light and polarization sensitivity of the detector.

The above measurements are not fully adequate to infer the blaze angle, as these fits are heavily based on only two data points (114 and 170 Å). To further constrain our model, in Fig. 13(c) we show measurements taken as a function of angle at a wavelength of 114 Å. These derived relative efficiencies show a clear blaze peak near a 9° graze angle. These data are best fit by an assumed blaze angle of 3.3° (or 2.8° with the alternate theory) and an efficiency of 82% (88%) times the theoretical values. Figure 13(d) shows the zero-order relative efficiencies and the theoretical curve times a factor of only 1.06. This is additional indication that very little of the diffracted light (6%) is misallocated from other orders and into the zero order.

From the measurements displayed in Fig. 13, we can confidently infer several things: (1) that the total energy diffracted into the grating orders equals the reflectance of the coating at the graze angle incident to the groove facets, (2) that in excess of 80% of the efficiency expected from perfectly formed grooves has been recovered, and (3) that the blaze angle is between 2.8° and 3.5° , in agreement with the specified value of 3.0° .

C. Background Suppression

Contamination of the spectrum by unwanted light can originate both within the instrument (e.g., order confusion) and externally (e.g., diffuse sky glow). However, these photons will be obstructed in three stages prior to reaching the detector. First, any light attempting to enter the instrument aperture from a sky position located outside the collimator field will be rejected by the medium and long wavelength channels. This causes diffuse sky lines to be restricted to narrow regions of the spectrum. At very large angles away from

Table II. Important Nightglow Features

| Wavelength Å | Transition | Average intensity | Shadow intensity |
|-----------------|---------------|-------------------|------------------|
| | | (entire sky) R | (ecliptic) R |
| 256 | HE II | 0.1 | — |
| 304 | HE II + O III | 12 | <0.02 |
| 584 | HE I | 3 | 3 |
| 600 | O III | 0.1 | — |
| 703 | O III | 0.2 | — |
| 718 | O II | 0.4 | — |
| 834 | O II + O III | 6 | 1.3 |
| 911 | O I | 1.5 | 1.5 |
| 938 | H I | 0.1 | <0.06 |
| 950 | H I | 0.4 | <0.06 |
| 972 | H I | 0.5 | <0.06 |
| 991 | N III + O I | 0.6 | <0.06 |
| 1025-1027 | O I + H I | 8.8 | 8.8 |
| 1216 | H I | 3500 | 3500 |
| 1304 | O I | 7 | 7 |

the optical axis, this is complemented by baffles within the telescope. Second, the low level of grating scatter expected (see Sec. III.B) prevents wavelengths from straying outside their intended spectral bin. Third, any remaining light reaching the focal plane from outside the spectral band will be largely removed by filters. Each of these three barriers permits only a small fraction (10^{-5} – 10^{-3}) of the undesired light to be transmitted and in combination remove almost all the background.

1. Collimators

The spectrum of a point source will be contaminated by diffuse night sky glow present in the geocoronal and interplanetary mediums, due dominantly to backscattered solar radiation. In Table II we list the dominant features of which these emissions are composed and the values of their nighttime intensities in units of Rayleighs ($1 \text{ R} = 10^6/4\pi \text{ photons/cm}^2/\text{sec/s}$) which we have used in determining our instrument background. The shadow intensities above 304 Å are representative of measurements taken while viewing down the earth's shadow cone from an uplooking satellite in a polar orbit at 600 km.⁵⁶ The intense hydrogen Lyman- α line at 1216 Å lies outside the EUV and is thus removed by use of thin-film filters, as discussed below, and also lies in the wings of the grating scatter profile. However, helium lines at 304 and 584 Å are also present in sufficient flux (10^0 – 10^1 R) to degrade the instrument sensitivity and unfortunately lie in the middle of the desired spectral region. At present there are no filters which can acceptably remove these lines and still provide suitable transmission at nearby wavelengths. However, we may confine these features to narrow regions of the point-source spectrum by a field stop. In the absence of a slit, we employ an array of wire grid collimators⁵⁷⁻⁵⁹ in the medium and long wavelength spectrometer channels (Fig. 1). These collimators have a triangular response for transmission of off-axis rays:

$$T(\theta, \phi) = T(0)[1 - |\cos\phi|\theta/\theta_c], \quad \theta/\theta_c < 1/\cos\phi \quad (12a)$$

$$= 0, \quad \Theta/\Theta_c > 1/\cos\phi, \quad (12b)$$

where Θ is the off-axis angle of a field point from the telescope optical axis, and ϕ is the azimuthal angle between the dispersion direction and the off-axis direction. We have employed a collimation full width at half-maximum Θ_c only in the dispersion direction of the grating. Thus if $\phi = \pi/2$ the radiation will not be attenuated at any off-axis angle, since the collimation is only in the normal direction. The 1-D collimation also permits minimum obstruction through the grid apertures and thus maintains high on-axis transmission $T(0)$, $\sim 70\%$.

Transmission of the desired light from a point source of radiation requires a pointing accuracy $\Theta_p < \Theta_c$. Averaging over all angles ϕ , the average transmission for the point source is

$$\langle T(\Theta) \rangle_\phi = T(0)[1 - (2/\pi)\kappa\Theta_p/\Theta_c], \quad (13a)$$

where

$$\kappa = 1, \text{ for } \Theta_p < \Theta_c, \quad (13b)$$

$$\kappa = 1 + \arccos(\Theta_c/\Theta_p)\theta_c/\theta_p - \sqrt{1 - (\theta_c/\theta_p)^2}, \text{ for } \Theta_p > \theta_c. \quad (13c)$$

We expect a satellite pointing capability $\Theta_p < 15$ min of arc during more than 50% of the observing time. (This corresponds to a 3σ pointing error of 35 min of arc for Gaussian errors distributed about $\Theta = 0$.) Adopting a collimator $\Theta_c = 20$ min of arc then ensures an average transmission in excess of $0.5 \times T(0)$.

Through a differential of the grating equation, one finds that the diffuse sky is restricted to a bounded spectral region λ :

$$\lambda_{\text{sky}} - D\lambda < \lambda < \lambda_{\text{sky}} + D\lambda, \quad (14a)$$

where

$$D\lambda \simeq -(d_0/m)(F/L_0)(\Theta_p + \Theta_c)\sin\alpha_0. \quad (14b)$$

Therefore, sky glow at 584 Å is confined to regions overlapping the point source spectrum from 522 to 646 Å, and sky glow at 304 Å similarly contaminates only the 273–335-Å region. Thus, the astrophysically important regions near 228 Å (He II edge) and 504 Å (He I edge) are immune from direct sky glow. In these uncontaminated regions (140–273, 335–380, 380–522, and 646–760 Å), the sensitivity rises by a factor of 5. If viewing down the earth's shadow, the intensity of the 304-Å glow drops to insignificant levels⁶⁰ (Table II), however the level of a 584-Å glow remains largely unchanged.⁶¹ Thus, the collimators significantly improve the general sensitivity of the medium and long wavelength channels.

Fabrication of a prototype 20-min of arc collimator is currently under way. To maintain the full sensitivity enhancement discussed above, a 1% upper limit is placed on the transmission leaks for incident angles $\Theta > \Theta_c$. This requires removal of transmission sidelobes out to $\pm 3^\circ$. The design employs an exponential spacing of intermediate grids in a coaligned stack, as originally proposed by Parkinson and also successfully employed by others.^{58,59} Each grid is chemically etched out of

molybdenum and is aligned relative to the stack by mechanical registers. Through a slight oversizing of the grid bars, transmission leaks due to misalignments can be virtually eliminated. In the extreme ultraviolet, transmission directly through the wire bars is negligible due to the EUV opacity of the material. However, collimator transmission outside the desired field can occur due to reflection pathways through the stack. These leaks must also be maintained below at 1% level, which should be directly attainable with this design.

A final consideration is diffraction through the narrow grid slots, which can broaden the collimator field of view.⁶² Each slot is of width

$$W = Z \tan\Theta_c, \quad (15)$$

where Z is the height of the collimator. A convenient estimate to this broadening⁶³ is given by the full width at half-maximum of the 1-D Fraunhofer pattern through an individual slot opening W :

$$\Delta\Theta_{\text{diffr}} = (2.8/\pi)\lambda/W. \quad (16)$$

With $Z = 150$ mm and $\Theta_c = 20$ min of arc, the slots are 850 μm wide. The wavelengths of interest are 140–760 Å which, from Eq. (16), introduce broadening in $\Theta_c < 0.3$ min of arc, in the collimator off-axis response. This effect is small enough to be neglected in the design. In principle, one might also consider the potential blurring of an incident stellar image due to slot diffraction. If each slot were positioned independently, one would expect an incoherent superposition of the response from a single opening, as given by Eq. (16). However, to maintain usable on-axis transmission through the stack of grids, the slots must be coaligned to an accuracy much finer than their individual widths. In practice, this is achieved with openings in any one grid being equally spaced except for random location errors which are not individually reproducible between different grids in the stack. The result is that each grid acts as a coherent array of apertures, i.e., a very coarse diffraction grating. Thus, in computing the blurring of an incident stellar image, i.e., the point-response function of the collimator, one should replace W in Eq. (16) by the total aperture of the collimator. Also being the aperture of the collecting optics, this diffraction limit is negligibly small. Even in the event of incoherent slots, the blurring of 0.3 min of arc is not a dominant contribution to the resolution budget of the instrument.

2. Filters

The use of collimators and a low level of grating scatter will remove most of the stray and diffuse light prior to reaching the focal plane. However, to safeguard against possible contamination by intense Lyman- α hydrogen glow (Table II), we also employ thin-film filters in front of the detector surfaces. Well-defined bandpasses are obtained by use of Parylene-N for channel A (70–190 Å) and aluminum for channels B (140–380 Å) and C (280–760 Å). The filter transmissions are obtained through use of the equation

$$T_{\text{filt}}(\lambda) = \exp[-\mu(\lambda)t], \quad (17)$$

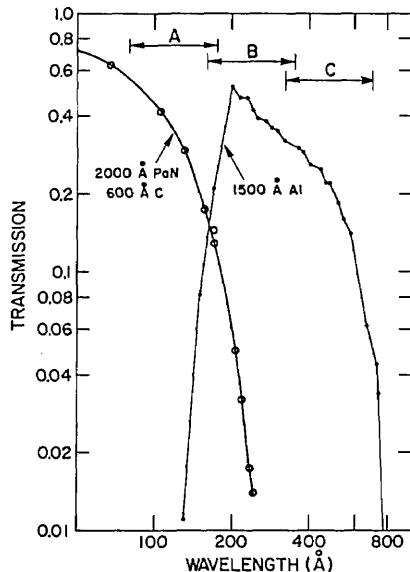


Fig. 15. Filter transmissions taken from Refs. 64 and 65. The range of each spectrometer channel is indicated at the top.

where t is the filter thickness, and $\mu(\lambda)$ are the linear absorption coefficients as given by Stern and Paresce⁶⁴ for Pa-N and by in-house data taken by Jelinsky⁶⁵ for aluminum and Pa-N. The filters are chosen with thicknesses capable of preventing a direct Lyman- α background from affecting the sensitivity limit for observing times $<40,000$ sec. This results in 3000 \AA of Pa-N and 1500 \AA of aluminum, each with transmissions at 1216 \AA of $<2 \times 10^{-5}$. The Pa-N filter also reduces most of the background in channel A due to HE II 304-\AA diffuse light. The measured filter transmissions within the intended EUV bands are plotted in Fig. 15, being typically 30–40% including the transmission (80%) from supporting nickel meshes. We note that a 3000-\AA Pa-N filter is of comparable transmission with the measured filter of 2000-\AA Pa-N with an additional 600 \AA of carbon on the front surface. Since the filters need not assume all the responsibility for background removal, a factor of 2 improvement in these transmissions is possible by use of thinner filters (2000-\AA Pa-N and 1000-\AA aluminum), which are however more susceptible to developing pinholes.

D. Focal Plane

The dispersed spectra will form a linear array of wavelengths which must be spatially resolved at $100 \mu\text{m}$ over a 50-mm aperture. To obtain the desired resolution and sensitivity, we must be able to follow the instrument pointing through time tagging of the photon arrivals. This requires single-photon counting to permit an accurate mapping of focal plane pixel with sky position and thus determination of absolute wavelength. To obtain high sensitivity, we also desire a detector quantum efficiency of 20% or higher and low background rates (<0.5 counts/cm²/sec).

These properties are met with microchannel plate detectors.^{66,67} Siegmund *et al.*⁶⁸ have described laboratory results on a prototype EUVE detector which already attains the desired levels of performance outlined

above for the EUVE spectrometer. The design takes advantage of a simple wedge-and-strip anode readout system.⁶⁹ Somewhat enhanced resolution ($50 \mu\text{m}$) may be obtained in the dispersion direction of the spectrometers while maintaining the same overall number of pixels. The spectroscopy detectors will also utilize CsI photocathodes for enhancement of the EUV quantum efficiency⁷⁰ to $\sim 30\%$. We note that a similar microchannel plate detector system has been measured in-flight¹⁶ to generate an internal background of 0.5 counts/cm²/sec.

IV. Instrument Performance

Returning to the system flow chart presented in Fig. 3, we can now take a quantitative inventory of all the contributions to the imaging and efficiency of the spectrometer. Following these two exercises (Secs. A and B, respectively), we derive the net sensitivity of this instrument for stellar observations (Sec. C).

A. Resolution

The resolution budget is dominated by an assumed pointing reconstruction with an error profile FWHM = 1 min of arc. Almost as large a contributor is the grating aberration, limiting the spectral resolution to $\lambda/\Delta\lambda = 200\text{--}350$ and the spatial resolution to $0.2\text{--}0.4$ mm ($0.5\text{--}1.0$ min of arc). The next largest aberrations are those due to detector pixels (FWHM of 0.1 mm = 0.5 min of arc in the dispersion plane), mirror off-axis aberrations (0.25 min of arc), and mirror on-axis aberrations (0.1 min of arc). Image blurring induced by misalignments is expected to be very small, corresponding to <0.1 min of arc.

In the event that the instrument pointing reconstruction is significantly better than assumed (e.g., is 10 sec of arc) and that the detector pixels are redistributed to optimize for spectroscopy ($50 \times 200\text{-}\mu\text{m}$ pixels over a 1024×256 format), we will essentially achieve the inherent grating resolution limits. However, if all the above aberrations do indeed arise, we must perform a convolution of terms which are dominant and comparable in magnitude. This calculation must include the 1-D projections of the aberration profiles. Several of the terms described above are accurately described as normal Gaussian error distributions, such as pointing reconstruction and detector pixels. However others, such as grating aberrations and off-axis mirror aberrations, are more accurately modeled as uniformly distributed errors within a sharp boundary.

The convolution of Gaussian distributions is simply a summation in quadrature of the component terms. The 1-D projection of a 2-D Gaussian is also a Gaussian with the same σ , which facilitates the computation. However, the convolution of two uniform and bounded distributions is a trapezoid with a FWHM equal to

$$U = u_{\max} + (1/2)u_{\min}, \quad (18a)$$

and the generalized result for the convolution of several such square waves is

$$U = u_1 + (1/2) \sum_{i \neq 1} u_i = (1/2) \left(u_1 + \sum_{\text{all } i} u_i \right), \quad (18b)$$

where $u_1 = u_{\max}$. To estimate the net aberrations in our instrument, we first separately sum the Gaussian terms and the uniform terms. This results in $2.355\sigma = 1.12$ min of arc and $U = 1.0$ min of arc near the spectrum center. As the second convolution is dominated by a single term (grating aberrations), we may accurately approximate this sum as a uniform distribution with a FWHM $= U$. This allows the final convolution to be written as a familiar probability distribution:

$$P(x) = \int_{\alpha_2}^{\alpha_1} \exp(-1/2\alpha^2) d\alpha, \quad (19)$$

where $\alpha_1 = (x - U/2)/\sigma$ and $\alpha_2 = (x + U/2)/\sigma$, for which excellent analytical approximations exist. Inserting the above values for σ and U , we find that $P(x)$ has a FWHM equal to $\Delta\theta$ of 1.25 min of arc. From Eq. (4), where the average resolution across each channel is

$$\langle \lambda/\Delta\lambda \rangle \approx 250/\Delta\theta \text{ (min of arc)}, \quad (20)$$

we find a spectral resolution of ~ 200 . As the grating dispersion increases with wavelength within each channel, the spectral resolution also increases with wavelength. In Fig. 16 we plot the dependence of this resolution on the wavelength for the three spectrometer channels. Although these values meet the basic science requirement for resolution, there is room for further improvement. For example, we also include in this figure the result which is obtained given enhanced pointing reconstruction (10-sec of arc FWHM) and detector pixels ($50 \mu\text{m}$ in the dispersion direction). In this case, the average resolution is 300.

Calculation of the net spatial resolution proceeds in an identical manner, except to recall that (1) the grating does not deamplify sky angles in the direction normal to dispersion, resulting in an aberration of only 0.25 min of arc for a 0.1-mm pixel height, and (2) the grating contributes 0.2–0.4 mm = 0.5–1 min of arc in the image heights. Thus, $2.355\sigma \approx 1.03$ min of arc and $\langle U \rangle \approx 1.15$ min of arc, yielding a net FWHM of ~ 1.5 min of arc. This spatial resolution capability greatly reduces the instrument background and provides simultaneous observation of multiple sources within the field of view.

B. Effective Area

The net collecting area of each spectrometer channel is the product of the geometric aperture and several efficiency factors. Listing these in their order of occurrence in the instrument optical pathway, we have

$$A(\lambda, m, \theta) = A_{\text{geom}} \times T_{\text{coll}}(\theta) \times R(\lambda, p) \times \epsilon_{\text{rel}}(\lambda, m) \times T_{\text{filt}}(\lambda) \times QE, \quad (21)$$

where $T_{\text{coll}}(\theta)$ is the collimator transmission at an off-axis angle θ , $R(\lambda, p)$ is the net reflectance curve of the three-bounce optical system as a function of the linear polarization p of the incident light, $\epsilon_{\text{rel}}(\lambda, m)$ is the relative grating efficiency curve for spectral order m , $T_{\text{filt}}(\lambda)$ is the filter transmission curve, and QE is the detector quantum efficiency. In writing Eq. (21), we have made several simplifying assumptions regarding

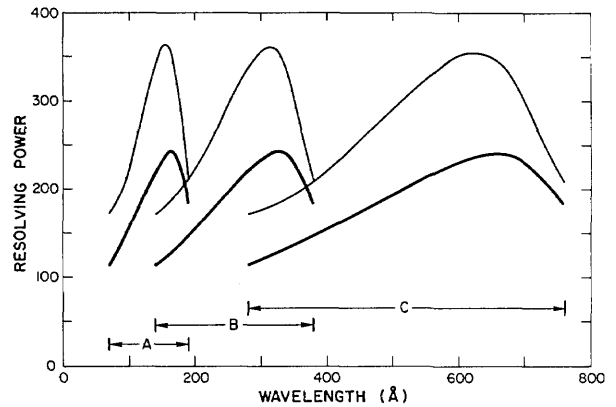


Fig. 16. Spectral resolution as a function of wavelength including all aberrations of the flight spectrometer. Upper (light) curves assume a satellite pointing reconstruction of 10 sec of arc, while the lower (dark) curves assume this is 1 min of arc.

the functional dependences. For example, we do not expect the collimator transmission to depend strongly on wavelength or polarization of the incident beam. Nor do we find the reflection coefficient of the optics to alter significantly as a function of the off-axis angle. For convenience, we also assume that the detector efficiency is a constant for the purposes of this calculation.

The geometric area devoted per spectrometer channel is 75.4 cm^2 , representing exactly one-sixth of the total primary mirror aperture of 452 cm^2 . Thus, the goal of 0.3 cm^2 can be met only if the net efficiency of this instrument is $>0.5\%$.

Collimators are necessary only in the medium and the long wavelength channels. Each collimator is designed to transmit at least 60% on-axis, which includes obstruction from supporting structures within the wire grids. The off-axis angle of the spectroscopy target is dominated by the choice of orbit platform for the EUVE mission. The outcomes range from a 1-min of arc capability (dominated by alignment errors between the instrument and the satellite) to a 15-min of arc average pointing error. Use of Eq. (13) then translates these values into net average transmissions of 58% and 31%, respectively. We include these two limiting cases separately in our calculations.

Due to the near planarity of the reflecting surfaces in the mirror-grating system (Fig. 17), the net reflection coefficient is approximately

$$R(\lambda, p) = (1/2)S(\lambda)[(1 - p)_{\sigma}R_{M1}(\lambda)_{\sigma}R_{M2}(\lambda)_{\sigma}R_G(\lambda) + (1 + p)_{\pi}R_{M1}(\lambda)_{\pi}R_{M2}(\lambda)_{\pi}R_G(\lambda)], \quad (22)$$

where the reflectances R are derived from the Fresnel equations, p is the linear polarization of the incident light, and $S(\lambda)$ is the fraction of reflected intensity which appears in the specular direction. If the electric vector is aligned along the mirror and grating tangents (TE = σ polarization), $p = -1$, while the orthogonal case (TM = π polarization) requires $p = +1$. Unpolarized incident light corresponds to $p = 0$. In the latter case, the primary and secondary mirror elements will none-

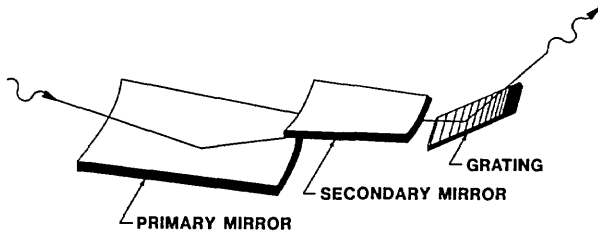


Fig. 17. Three-bounce reflection system of the EUVE spectrometer. Each channel uses only one-sixth of the telescope surface of revolution, resulting in a nearly plane-parallel alignment of the reflections. This significantly improves the net reflection coefficient.

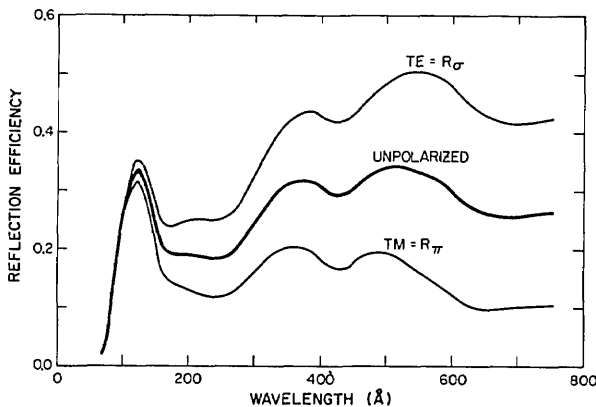


Fig. 18. System reflection coefficient for three states of linear polarization of the incident light using the optical alignment indicated in Fig. 17. The spectrometer reflection efficiency oscillates between the extreme case values for each 90° spin of the instrument about the line of sight.

theless induce a linear polarization into the beam. Using published optical constants³⁸⁻⁴⁰ for gold (mirrors) and rhodium (gratings), this separation of the polarization components results in significant enhancement (a factor of ~ 2) in the reflective throughput, compared to a naive calculation based on reflection coefficients for unpolarized light. In the event that the incident light is itself already linearly polarized, inspection of Fig. 18 reveals a strong relation between $R(\lambda)$ and the direction of that polarization ($p = -1$ or $p = +1$).

Thus, although not designed with this capability in mind, the spectrometer can also function simultaneously as a polarimeter. If during an observation the instrument were to be set into a slow spin about the optical axis, the direction of an incident linear polarization would oscillate between the TE and TM modes with a cycle of one-half the spin period. Of course, the observed modulation would also need to be deconvolved from the signal modulations caused by the collimator [Eq. (12)].

The specular fraction $S(\lambda)$ is derived from the expressions⁷¹

$$S(\lambda) = S_1(\lambda)S_2(\lambda)S_3(\lambda), \quad (23a)$$

$$S_i(\lambda) = \exp[-(4\pi h_i \sin \gamma_i / \lambda)^2], \quad (23b)$$

where γ_i is the graze angle and h_i is the root-mean-

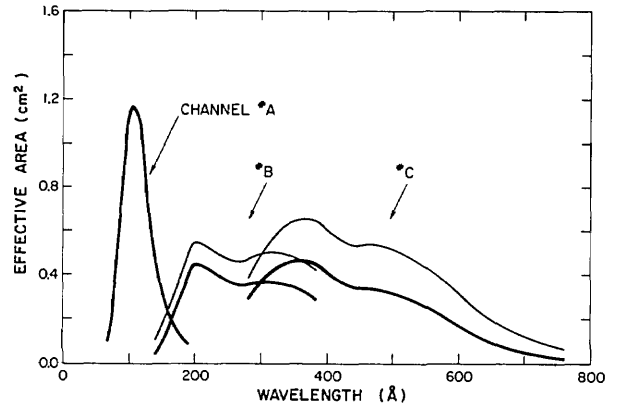


Fig. 19. Effective area as a function of wavelength for on-axis pointing toward a spectroscopy target. For off-axis pointing, these values are lowered as discussed in the text. The upper (light) curves assume a thinner aluminum filter (1000 \AA).

square (rms) surface height roughness for surface i . The fraction of reflected light which is scattered, $1 - S(\lambda)$, will be distributed in a halo centered at the specular image. Because part of this halo will be enclosed by the resolution element, Eq. (23) underestimates the usable fraction of the reflected light. However, we adopt this conservative approach and assume $h = 25 \text{ \AA}$ for each surface.

As we have made efficiency measurements on a sample EUVE grating (Fig. 13), we used these data as representative of $\epsilon_{\text{rel}}(\lambda)$ of the flight gratings. The wavelengths relevant to each channel are scaled from Fig. 13 by the groove densities for the three gratings, all having the same blaze angle.

For the filter transmission, we used the data^{64,65} from which Fig. 15 was derived. For the detector QE , we adopt a value of 30% as measured on microchannel plates⁷⁰ at these wavelengths. Due to soft x-ray absorption edges of the photocathode,³⁹ in practice there will be some dependence of the QE on wavelength, resulting in a dip near 200 \AA and an enhancement near 100 \AA .

In Fig. 19 we show the final result for the on-axis collecting area of the EUVE spectrometer. The design goal of $>0.3 \text{ cm}^2$ is met over the $80\text{--}600\text{-\AA}$ region, attaining significantly higher values over selected bands. The very high peak, over 1 cm^2 near 100 \AA , may be due to overestimated reflectance values there. At the longest wavelengths, $600\text{--}760 \text{ \AA}$, the low filter transmission results in a precipitous drop in area. This can be alleviated by use of a thinner aluminum filter (1000 \AA), as displayed in the upper (light) curves.

C. Sensitivity

Combining all the above-mentioned effects, one can calculate the sensitivity of this instrument. At each spectral bin, $\lambda \pm \Delta\lambda/2$, the minimum detectable flux for detection of spectral lines is

$$I_{\text{min}}(\lambda) = \frac{\sigma^2/2}{\tau A(\lambda)e} [1 + \sqrt{1 + (4/\sigma^2)B(\lambda)\tau}], \quad (24)$$

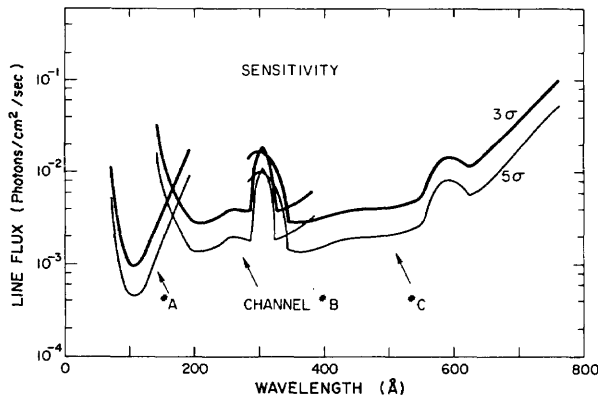


Fig. 20. Limiting sensitivity to spectral lines as a function of wavelength. The observing time was assumed to be 40,000 sec, and the detection threshold was set at 5σ (and 3σ). Dark curve is at the 5σ level (labels are incorrectly ordered). The bump in the sensitivity curve centered at 304 \AA disappears for observations of sources located down the earth's shadow cone.

where $A(\lambda)$ is the effective area at λ , τ is the observing time, σ is the sigma level of the detection (e.g., $\sigma = 5$ is a 5σ detection), e is the fractional energy encircled by a resolution element, and $B(\lambda)$ is the background rate. As a worst-case estimate for e , we consider the limiting spectral resolution FWHM. This corresponds to an aspect uncertainty of ~ 1 min of arc. The encircled energy from the mirror figure is essentially unity, as discussed above. If the image profile is dominantly a 2-D Gaussian and one integrates in the direction normal to dispersion ($\Delta\theta_y$), then $e = 0.76$ at the limiting spectral resolution and $e = 0.98$ at twice as coarse a resolution. We adopt $e = 0.76$ for all calculations.

We consider the case where there is no direct continuum from the cosmic source. The background rate per pixel is then

$$B(\lambda) = \alpha(\lambda)D + (10^6/4\pi)\Delta\theta_y\Delta\lambda \sum_i A(\lambda_i)J(\lambda_i) \times \int_{\theta_x} t_c(\theta)P(\lambda, \lambda_i, \theta)\delta\theta, \quad (25)$$

where $a(\lambda)$ is the image area at the detector, D is the detector background (counts/cm²/sec), $\Delta\theta_y$ is the image height projected on the sky ($\theta_y = H/F$), $\Delta\lambda$ is the spectral bin size, $J(\lambda_i)$ is the sky background (in Rayleighs) for emission line i (Table II), $t_c(\theta)$ is the relative collimator transmission at an off-axis angle θ in the dispersion direction, and $P(\lambda_{\text{diff}})$ is the point-response efficiency profile of the grating (in units of \AA^{-1}). The wavelength separation from the image center is

$$\lambda_{\text{sep}} \approx \lambda - \lambda_i \pm \theta(d_0/m)(F/L_0)\alpha_0. \quad (26)$$

The point-response function P can be decomposed into the geometrical aberration response (Fig. 6) and the scattering profile ω . If focused stray light dominates over hemispheric scatter, a convenient approximation is made on Eq. (25):

$$B(\lambda) \approx a(\lambda)D + \Delta\theta_y(10^6/4\pi) \sum_i A(\lambda_i)J(\lambda_i)[\langle\omega(\lambda_{\text{sep}})\rangle\Theta_c\Delta\lambda + t_c(\theta_\lambda)\Delta\theta_x], \quad (27)$$

where $\langle\omega(\lambda_{\text{sep}})\rangle$ is an effective average scattering factor over the range λ_{sep} from the image center [Eq. (26)] and where $\Delta\theta_x$ is the image FWHM in the dispersion direction. As defined previously, Θ_c is the collimator field full width at half-maximum. The angle θ_λ is the off-axis angle required in order that the incoming wave λ_i be diffracted to the wavelength bin λ . This angle is

$$\theta_\lambda = \alpha_0(L_0/F)[\sqrt{1 - 2m/d_0(\lambda - \lambda_i)/\alpha_0^2} - 1] \approx |m(\lambda - \lambda_i)|/d_0(L_0/F)\alpha_0. \quad (28)$$

The two terms within the brackets of Eq. (27) represent (1) the grating scatter of light integrated over the collimator field, and (2) the directly imaged light from an off-axis sky pixel.

The stray light level, $\langle\omega\rangle$, should be $<0.01\% \text{ \AA}^{-1} = 10^{-4} \text{ \AA}^{-1}$ from the distant 1216-\AA line (Table II) at any of the desired wavelengths from 70 to 760 \AA . To be conservative, we used a value of 10^{-3} \AA^{-1} in our calculations. With Eq. (27) and inserting the measures given previously for the individual terms contained therein, in Fig. 20 we plot the limiting sensitivity of the EUVE spectrometer in the three channels as a function of wavelength. These curves assume a 5σ detection threshold and an observing time of 40,000 sec. Background is a significant factor within the collimator transmission bumps near 304 and 584 \AA , the former being eliminated for observing lines of sight down the earth's shadow cone. Outside these bands, the sensitivity is simply equal to $\sigma^2/\tau/A(\lambda)/e$ from Eq. (24). An optimal sensitivity value is 10^{-3} photons/cm²/sec. The sensitivity curves can be easily converted into continuum flux units by the transformation

$$F_{\text{min}}(\lambda) = h(\lambda/\Delta\lambda)I_{\text{min}}(\lambda), \quad (29)$$

where $\lambda/\Delta\lambda$ may be lowered, to provide better sensitivity, by binning the data following an observation.

V. Applications

The sensitivity of the spectroscopy instrument is most usefully illustrated by way of simulated observations on example targets. At present only a sparse sample of data exists on extrasolar EUV sources.^{1-4,6-8} It is the primary function of the EUVE mission to survey the sky and generate a complete catalog of these sources. These data will be invaluable in identifying the brightest targets for the subsequent spectroscopic observations performed by EUVE and by other follow-on missions. This exploratory nature precludes an exhaustive or even representative listing of the objects likely to provide useful spectra. However, it is illustrative to at least consider the quality of spectra which can be estimated for the few classes of EUV sources presently known. In this section, we consider two such objects: hot white dwarfs and stellar coronas.

A. Hot White Dwarfs

White dwarf stars have been studied extensively at visual and ultraviolet wavelengths.^{72,73} The hot white

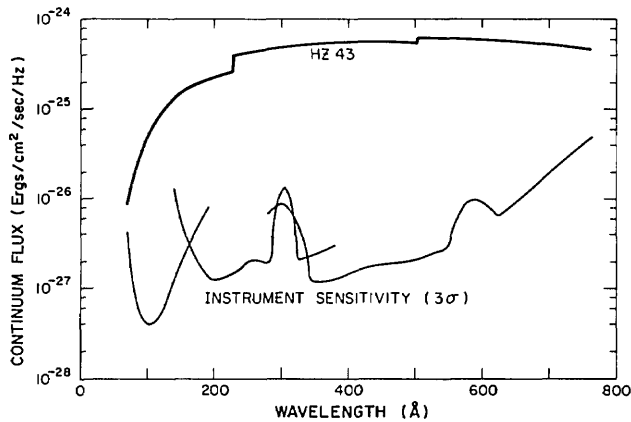


Fig. 21. Continuum flux from a known EUV source, HZ43, as a function of wavelength. This is compared to the limiting 3σ spectrometer sensitivity after a 40,000-sec observation, assuming a wavelength-binding resolution of $\lambda/\Delta\lambda = 100$. Sources approximately a factor of 100 dimmer than HZ43 will still be spectroscopically detectable.

dwarfs were the first extrasolar objects discovered at EUV wavelengths.^{1,2,6,7} Due to their bright continua, these stars are likely to serve as in-flight calibration standards for the EUVE scanning telescopes and the spectrometer. Extensive EUV observations^{1,6,8} exist for one hot white dwarf, HZ43. These data can be used to constrain several model parameters (temperature, density, and helium abundance) as well as the source distance and the intervening interstellar absorption. We have used a white dwarf atmosphere's code⁸ to generate Eddington surface fluxes, $H(\lambda)$, for HZ43. The surface flux at the earth can then be calculated:

$$F(\lambda) = 4\pi H(\lambda)(R_*/D)^2 \exp[-\sigma(\lambda)N_H], \quad (30)$$

where D is the distance to the source (65 pc), R_* is the star's radius (8.4×10^8 cm), N_H is the column density of neutral hydrogen along the line of sight, and $\sigma(\lambda)$ is an effective atomic cross section per neutral hydrogen atom in the interstellar medium. The atomic cross sections $\sigma(\lambda)$ were taken from Cruddace *et al.*⁷⁴ for cosmic elemental abundances, and a value of $N_H = 2 \times 10^{17} \text{ cm}^{-2}$ was adopted⁸ along the line of sight. To determine the ability to spectroscopically detect small amounts of helium, we included a fraction of 2×10^{-5} helium in the atmosphere.

In Fig. 21 we show these results compared to the sensitivity of the EUVE spectrometers [Eqs. (24) and (29)] after 12 h of observing. This plot reveals an EUV sensitivity ~ 2 orders of magnitude fainter than HZ43 from 100 to 600 Å. If even trace amounts of helium are present in the stellar atmosphere, they should be easily detectable in absorption at 228 Å. A raw count spectrum [Fig. 22(a)], which includes Poissonian counting statistics, also reveals the presence of an interstellar helium edge (504 Å). As another example, in Fig. 22(b) we show a simulated observation of another known hot white dwarf, G191-B2B,^{6,7} after a 20,000-sec exposure. The higher column density of hydrogen ($8 \times 10^{17} \text{ cm}^{-2}$) and thus helium along the line of sight to this source

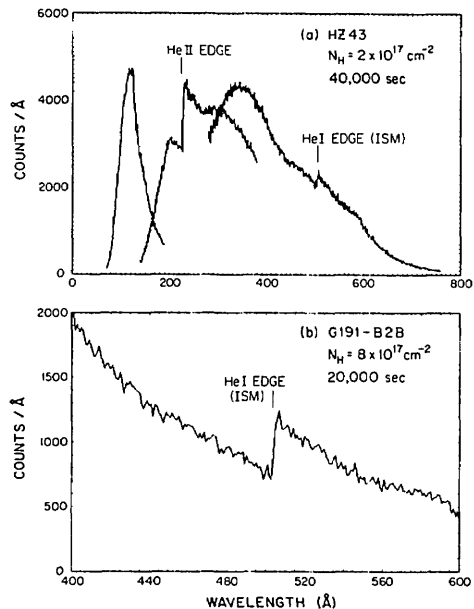


Fig. 22. Accumulated counts per $\Delta\lambda = \lambda/100$ bin for observations of two hot white dwarfs: (a) HZ43 for 40,000 sec, and (b) G191-B2B for 20,000 sec. The smooth bumps and the long wavelength decline are primarily due to the instrument effective area as plotted in Fig. 19. The noise is due to Poissonian counting statistics. The lower panel shows only a part of the long wavelength spectrometer channel near a simulated interstellar helium edge at 504 Å.

provides an excellent measure of a HE I interstellar edge at 504 Å. The broad EUV continuum shape is also very sensitive to the abundance of neutral hydrogen and thus several pieces of information on both the white dwarf and the interstellar medium are accessible through EUV spectroscopy. The predicted space densities of hot white dwarfs⁷⁵ and measured interstellar hydrogen column densities^{76,77} should permit a fair sample of such objects for EUVE spectroscopy.

B. Stellar Coronas

Hot plasmas surround several types of star, producing strong line emissions in the EUV³ and soft x-ray⁷⁸⁻⁸³ bands. An estimate to the EUV brightness of these sources can be obtained from EUV observations of line emission in the solar corona^{84,85} scaled by the ratio of measured broadband quiescent luminosities in the soft x ray, LSX:

$$I_*(\lambda) = I_\odot(\lambda)LSX_*/LSX_\odot/4.2 \times 10^{10}/D(\text{pc})^2 \exp[-N_H\sigma(\lambda)], \quad (31)$$

where $I_\odot(\lambda)$ are the measured solar line intensities at the earth (in units of 10^6 photons/cm²/sec), $I_*(\lambda)$ are the predicted source line intensities (photons/cm²/sec) at the earth, and the other quantities have been defined previously.

As an example, we consider the RS CVn source HR1099^{80,81,86,87} for which $LSX_*/LSX_\odot \approx 9000$, $D \approx 33$, and $N_H \approx 5 \times 10^{17} \text{ cm}^{-2}$. In Figs. 23(a)-(c) we show the raw counts of the predicted spectrum folded through the EUVE spectrometer and accumulated over 20,000 sec of observation. As in the previous example, back-

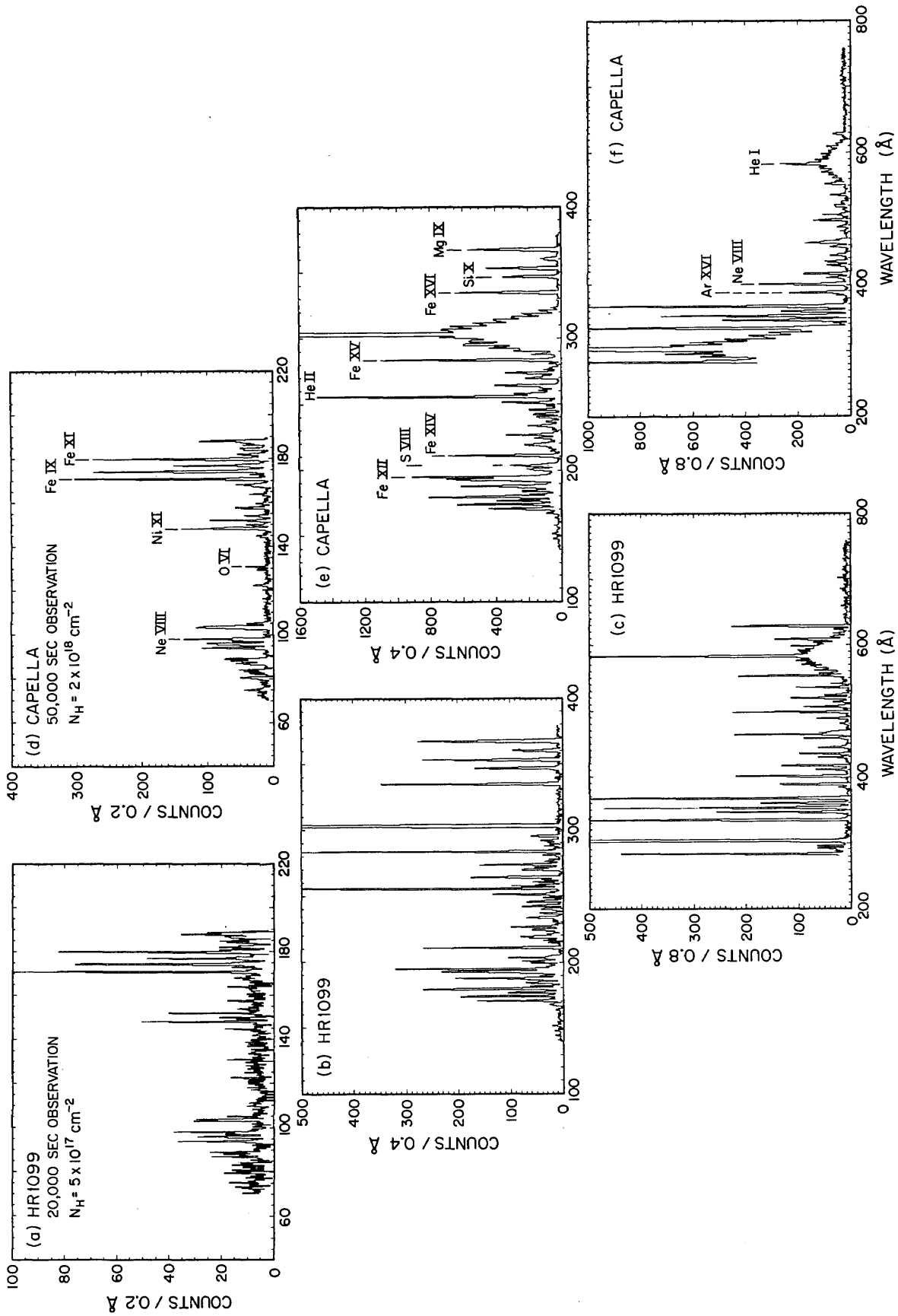


Fig. 23. Accumulated counts for observations of two coronal sources: (a)–(c) HR1099 after 20,000 sec down the earth's shadow, and (d)–(f) Capella after 50,000 sec. The lines observed in the short wavelength channel are sensitive to the temperature of the corona, while those appearing in the long wavelength channel are sensitive to the interstellar extinction along the line of sight.

ground has been included in the simulation [Eq. (27)]. The multitude of lines dramatically illustrates the advantage of spectroscopy for observations of sources for which the emissions are concentrated into specific wavelength features. We note that during a flare⁸⁰ such a spectrum could be recorded in ~ 3000 sec. In Figs. 23(d)–(f) we also show the spectrum of another RS CVn star, Capella ($LSX_*/LSX_\odot \approx 3000$) after a 50,000-sec observation. Although the higher column density ($N_H \approx 2 \times 10^{18} \text{ cm}^{-2}$) to this source lowers the intensities observed in the long wavelength channel, the short wavelength features are prominent. In addition, such sources are known to have higher coronal temperatures ($\sim 10^7$ K) than does the sun, and thus our scaling [Eq. (31)] underestimates the intensities of the highly ionized short wavelength emissions. Other sources for which similar spectra are expected include dM stars^{78,79} and cataclysmic variables.⁴

VI. Conclusions

We have described the instrument design for the Extreme Ultraviolet Explorer spectrometer. The individual components of this design have been discussed in detail. A test grating has been characterized and performs as required in terms of efficiency and resolution. In the process we have demonstrated that varied line-space mechanically ruled gratings can attain levels of performance comparable with the highest quality conventional gratings. A laboratory experiment featuring the test grating has revealed performance very competitive with existing high resolution laboratory spectrographs.

Measurements of the grating performance have been included in calculations of the flight instrument's sensitivity and imaging properties. The resulting performance figures have been discussed in terms of resolution and sensitivity. Predicted emissions from extrasolar EUV objects have been folded through these performance curves and reveal readily detectable features of current scientific interest.

The authors would like to thank T. Harada for fabrication of the grating, J. Edelstein for invaluable technical support, and the staff of the Space Astrophysics Group without whom this project would not have been possible. We also thank A. Bunner and H. Shipman for helpful comments, B. Henke and C. Dittmore for supplying soft x-ray film, and C. Romanik and the Berkeley Astronomy Department for the use of a PDS microdensitometer. This work was funded by NASA contract NASW-3636.

References

1. M. Lampton, B. Margon, S. Bowyer, R. Stern, and F. Paresce, "Discovery of a Non-Solar Extreme Ultraviolet Source," *Astrophys. J.* **203**, L71 (1976).
2. B. Margon, M. Lampton, S. Bowyer, R. Stern, and F. Paresce, "An Intense Extreme Ultraviolet Source in Cetus," *Astrophys. J.* **210**, L79 (1976).
3. B. M. Haisch, J. L. Linsky, M. Lampton, F. Paresce, B. Margon, and R. Stern, "Extreme Ultraviolet Observations of a Flare on Proxima Centauri and Implications Concerning Flare-Star Scaling Theory," *Astrophys. J.* **213**, L119 (1977).
4. B. Margon, P. Szkjod, S. Bowyer, M. Lampton, and F. Paresce, "Extreme-Ultraviolet Observations of Dwarf Novae from Apollo-Soyuz," *Astrophys. J.* **224**, 167 (1978).
5. S. Bowyer, R. Malina, M. Lampton, D. Finley, F. Paresce, and G. Penegor, "The Extreme Ultraviolet Explorer," *Proc. Soc. Photo-Opt. Instrum. Eng.* **279**, 176 (1981).
6. J. B. Holberg, B. R. Sandel, W. T. Forrester, A. L. Broadfoot, H. L. Shipman, and D. C. Barry, "Extreme UV and Far-UV Observations of the White Dwarf HZ43 from Voyager 2," *Astrophys. J.* **242**, L119 (1980).
7. J. B. Holberg, "The Local Interstellar Medium," *Proc. Int. Astron. Union Coll.* **81** (Sept. 1984).
8. R. F. Malina, C. S. Bowyer, and G. Basri, "Extreme Ultraviolet Spectrophotometry of the Hot DA White Dwarf HZ43: Detection of HE II in the Stellar Atmosphere," *Astrophys. J.* **262**, 717 (1982).
9. B. R. Sandel, *et al.*, "Extreme Ultraviolet Observations from Voyager 2 Encounter with Jupiter," *Science* **206**, 962 (1979).
10. F. Paresce, "Compact Sources of EUV Radiation," *Earth Extraterr. Sci.* **3**, 55 (1977).
11. A. K. Dupree, "The Astrophysical Interest of EUV Observations of Extra-Solar Objects," *Space Sci. Rev.* **29**, 479 (1981).
12. M. C. Hetttrick, "Spectrometer Option Study," MCH/EUVE/321/82, U. California, Berkeley (1982).
13. H. A. Rowland, "Preliminary Notice of the Results Accomplished in the Manufacture and Theory of Gratings for Optical Purposes," *Philos. Mag.* **13**, 469 (1882); "On Concave Gratings for Optical Purposes," **16**, 197 (1883).
14. D. L. Garrett and R. Tousey, "Solar XUV Grazing Incidence Spectrograph on Skylab," *Appl. Opt.* **16**, 898 (1977).
15. J.-D. Bartoe, G. E. Brueckner, J. D. Purcell, and R. Tousey, "Extreme Ultraviolet Spectrograph ATM Experiment S082B," *Appl. Opt.* **16**, 879 (1977).
16. S. Bowyer, R. Kimble, F. Paresce, M. Lampton, and G. Penegor, "Continuous-Readout Extreme-Ultraviolet Airglow Spectrometer," *Appl. Opt.* **20**, 477 (1981).
17. J. H. Underwood and W. M. Neupert, "GSFC EUV and x-Ray Spectroheliograph on OSO-7," *Sol. Phys.* **35**, 241 (1974).
18. W. A. Rense and T. Violet, "Method of Increasing the Speed of a Grazing-Incidence Spectrography," *J. Opt. Soc. Am.* **49**, 139 (1959).
19. R. C. Chase, A. S. Krieger, and J. H. Underwood, "Grazing Incidence Relay Optics," *Appl. Opt.* **21**, 4446 (1982).
20. H. Gursky and T. Zehnpfennig, "An Image-Forming Slitless Spectrometer for Soft X-Ray Astronomy," *Appl. Opt.* **5**, 875 (1966).
21. T. Zehnpfennig, "Development of a Slitless Spectrograph for X-Ray Astronomy," *Space Sci. Rev.* **9**, 342 (1969).
22. J. H. Dijkstra, L. J. Lantwood, and C. Timmerman, "X-Ray Transmission Gratings," in *New Instrumentation for Space Astronomy*, K. A. van der Hucht and G. S. Vaiana, Eds. (Pergamon, London, 1978), p. 257.
23. K. P. Beuermann, H. Brauninger, and J. Trumper, "Aberrations of a Facet-Type Transmission Grating for Cosmic X-Ray and XUV Spectroscopy," *Appl. Opt.* **17**, 2304 (1978).
24. A. C. Brinkman, J. H. Dijkstra, W. F. P. A. L. Geerlings, F. A. van Rooijen, C. Timmerman and P. A. J. de Korte, "Efficiency and Resolution Measurements of X-Ray Transmission Gratings Between 7.1 and 304 Å," *Appl. Opt.* **19**, 1601 (1980).
25. P. Predehl, H. Brauninger, H. Kraus, and J. Trumper, "Fabrication of Transmission Gratings for Use in X-Ray Astronomy," *Proc. Soc. Photo-Opt. Instrum. Eng.* **316**, 128 (1981).
26. F. D. Seward *et al.*, "Calibration and Efficiency of the Einstein Objective Grating Spectrometer," *Appl. Opt.* **21**, 2012 (1982).

27. M. Stedman and B. Gale, in *Proceedings, X-Ray Optics Symposium, Mullard Space Sciences Laboratory of University College London, Holmbury St. Mary* (1973), pp. 122–136.
28. S. O. Kastner and C. Wade, Jr., "Aspheric Grating for Extreme Ultraviolet Astronomy," *Appl. Opt.* **17**, 1252 (1978).
29. M. C. Hettrick and S. Bowyer, "Varied Line-Space Gratings: New Designs for Use in Grazing Incidence Spectrometers," *Appl. Opt.* **22**, 3921 (1983).
30. M. C. Hettrick, "Aberrations of Varied Line-Space Grazing Incidence Gratings in Converging Light Beams," *Appl. Opt.* **23**, 3221 (1984).
31. H. Wolter, "Spiegelsysteme Streifenden Einfalls als abbildende Optiken für Röntgenstrahlen," *Ann. Phys.* **10**, 94 (1952); "(Generalized Schwarzschild Systems of Mirrors with Glancing Reflection as Optical Systems for X-Rays) Verallgemeinerte Schwarzschildsche Spiegelsysteme Streifender Reflexion als Optiken für Röntgenstrahlen," *Ann. Phys.* **10**, 286 (1952).
32. D. Finley, R. Malina, and S. Bowyer, "Fabrication of Mirrors for the Extreme Ultraviolet Explorer Satellite," in *Proceedings, Optical Fabrication Conference*, Space Flight Center, Greenbelt (Jan. 1985).
33. T. Harada and T. Kita, "Mechanically Ruled Aberration-Corrected Concave Gratings," *Appl. Opt.* **19**, 3987 (1980).
34. F. Paresce, S. Kumar, and C. S. Bowyer, "Continuous Discharge Line Source for the XUV," *Appl. Opt.* **10**, 1904 (1971).
35. B. L. Henke, S. L. Kwok, J. Y. Vejo, H. T. Yamada, and G. C. Young, "Low Energy X-Ray Response of Photographic Films. I. Mathematical Models," *J. Opt. Soc. Am. B* **1**, 818 (1984); B. L. Henke, F. J. Fujiwara, M. A. Tester, C. H. Dittmore, and M. A. Palmer, "II. Experimental Characterization," *J. Opt. Soc. Am. B* **1**, 828 (1984).
36. J. Edelstein, M. C. Hettrick, S. Mrowka, C. Martin, and P. Jelinsky, "Extreme UV Measurements on a Varied Line-Space Hitachi Reflection Grating: Efficiency and Scattering," *Appl. Opt.* **23**, 3267 (1984).
37. G. H. Mount and W. G. Fastie, "Comprehensive Analysis of Gratings for Ultraviolet Space Instrumentation," *Appl. Opt.* **17**, 3108 (1978).
38. J. T. Cox, G. Hass, and W. R. Hunter, "Optical Properties of Evaporated Rhodium Films Deposited at Various Substrate Temperatures in the Vacuum Ultraviolet from 150–2000 Å," *J. Opt. Soc. Am.* **61**, 360 (1971).
39. B. L. Henke, P. Lee, T. J. Tanaka, R. L. Shimabukuro, and B. K. Fujikawa, "Low-Energy X-Ray Interaction Coefficients: Photoabsorption, Scattering and Reflection," *Atom. Data Nucl. Data Tables* **27**, 1982; B. L. Henke, *Proc. Soc. Photo-Opt. Instrum. Eng.* **316**, (1981).
40. L. R. Canfield, G. Hass, and W. R. Hunter, "The Optical Properties of Evaporated Gold in the Vacuum Ultraviolet from 300 Å to 2000 Å," *J. Phys.* **25**, 124 (1964).
41. W. R. Hunter, D. W. Angel, and G. Hass, "Optical Properties of Evaporated Platinum Films in the Vacuum Ultraviolet from 2200 Å to 150 Å," *J. Opt. Soc. Am.* **69**, 1695 (1979).
42. B. L. Henke and M. L. Tester, "Techniques of Low-Energy X-Ray Spectroscopy (0.1–2 KeV Region)," *Adv. X-Ray Anal.* **18**, 76 (1975).
43. D. S. Finley, S. Bowyer, F. Paresce, and R. F. Malina, "Continuous Discharge Penning Source with Emission Lines Between 50 Å and 300 Å," *Appl. Opt.* **18**, 649 (1979).
44. H. A. Rowland, "Gratings in Theory and Practice," *Philos. Mag.* **35**, 397 (1883); *Astron. Astrophys.* **12**, 129 (1883); *Physical Papers of Henry A. Rowland* (Johns Hopkins U.P., 1902), p. 525–544.
45. R. D. Hatcher and J. H. Rohrbaugh, "Theory of the Echelette Grating. I," *J. Opt. Soc. Am.* **46**, 104 (1956); "Theory of the Echelette Grating. II," **48**, 704 (1958).
46. M. Nevire, D. Maystre, and W. R. Hunter, "Use of Classical and Conical Diffraction Mountings for XUV Gratings," *J. Opt. Soc. Am.* **68**, 1106 (1978).
47. D. Maystre and R. Petit, "Quelques Recents Resultats en Theorie des Reseaux: Application a Leur Utilization dans L'Extreme Ultraviolet," *Nouv. Rev. Opt.* **7**, 165 (1976).
48. D. Maystre and R.C. McPhedran, "Le Theorem de Reciprocite Pour Les Reseaux de Conductivite Finie: Demonstration et Applications" *Opt. Commun.* **12**, 164 (1974).
49. D. Maystre, M. Nevire, and R. Petit, "Experimental Verifications and Applications of the Theory," in *Electromagnetic Theory of Gratings*, R. Petit, Ed. (Springer, 1980), Chap. 6.
50. R. P. Madden and J. Strong, in *Concepts of Modern Optics*, J. Strong Ed. (Freeman, San Francisco, 1958), Appendix P, pp. 597–608.
51. A. P. Lukirskii and E. P. Savinov, "Use of Diffraction Gratings and Echelettes in the Ultra-Soft X-Ray Region," *Opt. Spektrosk.* **14**, 285 (1963); *Opt. Spektrosk.* **14**, 147 (1963).
52. D. L. Schroeder and R. L. Hilliard, "Echelle Efficiencies: Theory and Experiment," *Appl. Opt.* **19**, 2833 (1980); "Author's Reply to Comment," *Appl. Opt.* **20**, 530 (1981).
53. M. Bottema, "Echelle Efficiency and Blaze Characteristics," *Proc. Soc. Photo-Opt. Instrum. Eng.* **240**, 171 (1980); "Echelle Efficiencies: Theory and Experiment; Comment," *Appl. Opt.* **20**, 528 (1981).
54. S. Engman and P. Lindblom, "Blaze Characteristics of Echelle Gratings," *Appl. Opt.* **21**, 4356 (1982).
55. E. G. Loewen and M. Nevire, "Simple Selection Rules for VUV and XUV Diffraction Gratings," *Appl. Opt.* **17**, 1087 (1978).
56. S. Chakrabarti, R. Kimble, and S. Bowyer, "Spectroscopy of the EUV (350–1400 Å) Nightglow," *J. Geophys. Res.* **89**, 5660 (1984).
57. M. Oda, "High-Resolution X-Ray Collimator with Broad Field of View for Astronomical Use," *Appl. Opt.* **4**, 143 (1965).
58. R. L. Blake, P. F. Santos, D. M. Barrus, W. Brubaker, E. Fenimore, and R. Puetter, "Collimators for Soft X-Ray Measurements," *Space Sci. Instrum.* **2**, 171 (1976).
59. R. A. Nobles, L. W. Acton, E. G. Joki, J. W. Leibacher, and R. C. Peterson, "Large-Aperture High-Resolution X-Ray Collimator for the Solar Maximum Mission," *Appl. Opt.* **19**, 2957 (1980).
60. F. Paresce, H. Fahr, and G. Lay, "A Search for Interplanetary HE II, 304 Å Emission," *J. Geophys. Res.* **86**, 10,038 (1981).
61. F. Paresce, S. Bowyer, and S. Kumar, "Evidence for an Interstellar or Interplanetary Source of diffuse HE I 584 Å Radiation," *Astrophys. J.* **183**, L87 (1973).
62. R. L. Blake, D. M. Barrus, and E. Fenimore, "Diffraction Effects on Angular Response of X-Ray Collimators," *Rev. Sci. Instrum.* **47**, 889 (1976).
63. C. A. Lindsey, "Effect of Diffraction in Multiple-Grid Telescopes for X-Ray Astronomy," *J. Opt. Soc. Am.* **68**, 1708 (1978).
64. R. Stern and F. Paresce, "Mass Absorption Coefficients of Parlylene-N at Soft X-ray and Vacuum-Ultraviolet Wavelengths," *J. Opt. Soc. Am.* **65**, 1515 (1975).
65. P. Jelinsky, Space Sciences Laboratory; private communication (1982).
66. M. Lampton, "The Microchannel Image Intensifier," *Sci. Am.* **245**, 62 (1981).
67. O. H. W. Siegmund and R. F. Malina, "Detection of Extreme UV and Soft X-Rays with Microchannel Plates: A Review," in *Multichannel Image Detectors*, Vol. 2, Y. Talmi, Ed. (American Chemical Society, Washington, D.C., 1983), pp. 253–275.
68. O. H. W. Siegmund, R. F. Malina, K. Coburn, and D. Werthimer, "Microchannel Plate EUV Detectors for the extreme Ultraviolet Explorer," *IEEE Trans. Nucl. Sci.* **NS-31**, 776 (1984).
69. C. Martin, P. Jelinsky, M. Lampton, R. F. Malina, and H. O. Anger, "Wedge-and-Strip Anodes for Centroid-Finding Position-Sensitive Photon and Particle Detectors," *Rev. Sci. Instrum.* **52**, 1067 (1981).
70. C. Martin and S. Bowyer, "Quantum Efficiency of Opaque CsI

- Photocathodes with Channel Electron Multiplier Arrays in the Extreme and Far Ultraviolet," *Appl. Opt.* 21, 4206 (1982).
71. P. A. J. de Korte *et al.*, "EXOSAT X-Ray Imaging Optics," *Appl. Opt.* 20, 1080 (1981).
 72. J. Liebert, "White Dwarf Stars," *Ann. Rev. Astron. Astrophys.* 18, 363 (1980).
 73. R. F. Green, "The Luminosity Function of Hot White Dwarfs," *Astrophys. J.* 238, 685 (1980).
 74. R. Cruddace, F. Paresce, S. Bowyer, and M. Lampton, "On the Opacity of the Interstellar Medium to Ultra-Soft X-Rays and Extreme-Ultraviolet Radiation," *Astrophys. J.* 187, 497 (1974).
 75. D. Koester, "The Space Density of Hot White Dwarfs," *Astron. Astrophys.* 65, 449 (1978).
 76. F. C. Bruhweiler and Y. Kondo, "The UV Spectra of Nearby White Dwarfs and the Nature of the Local Interstellar Medium," *Astrophys. J.* 259, 232 (1982).
 77. P. C. Frisch and D. G. York, "Synthesis Maps of Ultraviolet Observations of Neutral Interstellar Gas," *Astrophys. J.* 271, L59 (1983).
 78. G. S. Vaiana *et al.*, "Results from an Extensive Einstein Stellar Survey," *Astrophys. J.* 244, 163 (1981).
 79. R. Rosner *et al.*, "The Stellar Contribution to the Galactic Soft X-Ray Background," *Astrophys. J.* 249, L5 (1981).
 80. N. E. White, P. W. Sanford, and E. J. Weiler, "An X-Ray Outburst from the RS CVn Binary HR1099," *Nature London* 274, 569 (1978).
 81. F. Walter, P. Charles, and S. Bowyer, "Discovery of Quiescent X-Ray Emissions from HR1099 and RS CVn," *Nature London* 274, 570 (1978).
 82. W. Cash, S. Bowyer, P. A. Charles, M. Lampton, G. Garmire, and G. Riegler, "The Soft X-Ray Spectrum of Capella: Discovery of Intense Line Emission," *Astrophys. J.* 223, L21 (1978).
 83. S. M. Kahn *et al.*, "HEAO-1 Observation of X-Ray Emission from Flares on dM₀ Stars," *Astrophys. J.* 234, L107 (1979).
 84. A. K. Dupree, M. C. E. Huber, R. W. Noyes, W. H. Parkinson, E. M. Reeves, and G. L. Withbroe, "The Extreme-Ultraviolet Spectrum of a Solar Active Region," *Astrophys. J.* 182, 321 (1973).
 85. M. Malinovsky and L. Heroux, "An Analysis of the Solar Extreme-Ultraviolet Spectrum Between 50 and 300 Å," *Astrophys. J.* 181, 1009 (1973).
 86. E. J. Weiler *et al.*, "Coordinated Ultraviolet, Optical, and Radio Observation of HR1099 and UX Arietis," *Astrophys. J.* 225, 919 (1978).
 87. F. M. Walter, W. Cash, P. A. Charles, and C. S. Bowyer, "X-Rays from RS Canum Venaticorum Systems: A HEAO 1 Survey and the Development of a Coronal Model," *Astrophys. J.* 236, 217 (1980).

Patter continued from page 1718

laser as the monochromatic source, which is focused onto the input ends of two single-mode fibers having nominal 4.5- μm diam cores. The external plastic jacketing and inner RTV (room-temperature-vulcanized) sleeving are removed from the first several centimeters of both ends of both fibers, and ~ 4 cm of exposed fiber are painted with index-matching mode-stripping fluid. Approximately 2.5 cm at the ends of each fiber are not painted. The sample and reference optical signal are optically recombined, spatially filtered, and detected through an electronic output signal proportional to the instantaneous stress in the fiber.

This work was done by John H. Cantrell, Jr., of Langley Research Center and Richard O. Claus, Janet C. Wade, and Paul S. Zerwekh of Virginia Polytechnic Institute and State University. Refer to LAR-12965.

Acoustic Gaussian far-field pattern

A new ultrasonic transducer produces a far-field beam with a Gaussian spatial profile for materials evaluation. The transducer is constructed by depositing a circularly symmetric metallic multielectrode array on a 12.7-mm diam X-cut quartz disk. Each electrode is independently connected to an impedance network optimized to produce the Gaussian distribution with less than 2% error.

An electric-field distribution that is exclusively a function of radius is produced by the set of concentric ring electrodes. If the circumstances of the rings are large with respect to the spacing between successive electrodes, the electric field in the gaps may be considered a linear function of radius. From this model, a piecewise linear function that approximates the Gaussian may be then generated on the face of the piezoelectric crystal by applying proper voltages to the electrodes. The degree to which this function fits the desired Gaussian is determined by the width of each electrode ring, the number of electrodes, and the distribution of the electrode radii on the radius of the transducer crystal.

Because the ideal Gaussian voltage distribution is a smooth function of the radius, the electrode width should be as small as possible. The photoetching techniques used, however, required a minimum electrode width of ~ 0.5 mm. The degree of fit to the desired Gaussian shape may also be improved by using a large number of electrodes; but this approach requires that the interelectrode spacing be small, thereby increasing the possibility of electrical breakdown between adjacent rings when high voltages are applied.

Considering these practical limitations, it was found that, with as few as five electrodes, the mean absolute fit error may be reduced to less than 1.5% of the peak. Because the radii of the rings are the variables over which greatest control may be exercised during design, an iterative computer routine was developed to minimize absolute error by varying ring placement.

The designed electrode pattern was photoetched onto a layer of chromium and gold on a circular 2.25-MHz X-cut quartz transducer. Capacitance between electrodes and the wear-plate ground plane was calculated and later empirically verified to be less than 2 pF, producing a negligible reactive impedance at the 2.25-MHz operating frequency. Because this impedance is low, a simple resistive network may be used to fix the desired set of electrode voltages.

Construction details of the transducer are shown in Fig. 8. The leads are attached to the electrodes with a conductive adhesive, and a dome of epoxy is applied to the electrode side of the crystal to provide mechanical support for the leads and to attenuate and disperse resonant surface-wave modes. Further damping is accomplished by a thin semiviscous layer of electrically conductive adhesive placed on the opposite uncoated side of the transducer disk and under a thin aluminum-foil electrode/wear plate. The electrode leads are connected to the resistive network and coaxial cable, and the entire transducer assembly is placed in a 1.3-cm i.d. cylindrical PVC (polyvinyl chloride) case and potted in filler-loaded epoxy.

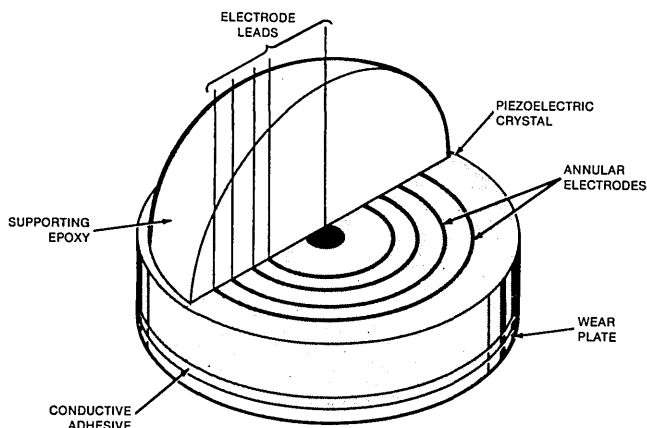


Fig. 8. Concentric electrode rings in the ultrasonic transducer produce a beam with a Gaussian profile. The transducer is used for materials evaluations.

This work was done by Richard O. Claus and Paul S. Zerwekh of Virginia Polytechnic Institute and State University for Langley Research Center. Refer to LAR-12967.

continued on page 1760